Politecnico di Torino

Politecnico di Torino

Facoltà di Ingegneria
Dipartimento Energia *Galileo Ferraris*

Corso di Laurea Magistrale in
Ingegneria Energetica e Nucleare - Sustainable Nuclear Energy

Magnetohydrodynamic Stability of Negative Triangularity Plasmas

Coordinator:
Prof. Fabio Subba

Supervisors:
Dr. Tommaso Bolzonella
Dr. Leonardo Pigatto

Student:
Anthony Piras

Torino, Academic Year 2021/2022

A C K N O W L E D G M E N T S

Throughout the writing of this dissertation I have received a great deal of support and assistance.

I would first like to thank my supervisor, Prof. Fabio Subba, whose expertise was invaluable in formulating the research questions and methodology.

I would also like to acknowledge those who looked after me during my internship at Consorzio RFX. I would particularly like to single out my supervisor Dr. Tommaso Bolzonella. I want to thank him for his patient support and for all of the opportunities I was given to further my research.

I would also like to thank my tutor, Dr. Leonardo Pigatto, for his valuable guidance throughout my studies. He provided me with the tools I needed to choose the right direction and successfully complete my dissertation.

DEDICATION

Le persone capitano per caso
nella nostra vita,
ma non a caso.
— Alda Merini, *Le persone capitano per caso*

Ai miei genitori. Per esserci sempre, da sempre e, ne sono convinto, per sempre.

Agli amici di sempre, partiti e ritrovati, che da anni mi accompagnano in questo strano viaggio che è la vita, per il costante supporto e sprone a non arrendermi. Menzione speciale per Manuel, mio coinquilino in quel di Torino, per le risate strappate durante le lezioni online, in un periodo difficile, e per i meme nati al calar del sole. *Quando cala il sole, calano le maschere.*

Alle amiche ed agli amici degli anni universitari, vecchi e nuovi, per le serate infinite, per i pranzi, per le cene, per aver colorato il grigio di Torino e della mia vita durante gli anni più importanti. Anche se non ci siamo più visti per ovvie ragioni, sappiate che vi sento sempre al mio fianco.

A Sara, per avermi mostrato cosa voglia dire essere forti ed al contempo calmi, quasi stoici, di fronte alle situazioni più avverse.

A Claudia. Per il tempo che mi ha dedicato, per il supporto e la comprensione. Per l'amore dato, a volte non corrisposto. *E sempre, come un amuleto, tengo i tuoi occhi nella tasca interna del giubbotto.*

Alla Prof.ssa Fabiola Freddi, per aver indirizzato la mia vita sul sentiero che mi ha portato dove sono oggi.

A tutte le *ragazze che seguivo*, e che adesso, per qualche strana ragione, sembra mi stiano perseguitando.
A chi ha lasciato qualcosa di immateriale, che porterò sempre dentro.
A chi ha condiviso il proprio mondo, la propria terra, il proprio mare, l'odore del suo paese con me.
A chi non è stata, e chissà cosa avrebbe potuto essere.

ABSTRACT

The aim of this work is to investigate the stability of negative triangularity, magnetically confined plasmas. The work is carried out at Consorzio RFX and within the framework of EUROfusion *Tokamak Exploitation Work Package*.

The chief reason behind this investigation is the recent rise in the interest surrounding negative triangularity plasmas, seeing that they seem to be more stable and lead to power losses lower than positive triangularity while requiring less net auxiliary power to reach an acceptable confinement.

The stability properties of different plasmas are explored starting from the RFX-mod shaped tokamak results and exploring projections to negative triangularity. Recent discharges of the TCV experiment are then analyzed, comparing stability properties between negative and positive triangularity plasmas. This comparative analysis is carried out by means of two different codes, namely CHEASE and MARS-F; the first being an equilibrium code which solves the Grad-Shafranov equation in weak form, and the second one a linear resistive-MHD code which solves the linear stability of a plasma.

Results obtained by numerical modeling of real plasma discharges showed that triangularity can indeed play a role in stabilizing the resistive modes both for low-q_0 and high-q_0 plasmas, while it does not significantly affect the structure and dynamics of ideal modes.

CONTENTS

LIST OF FIGURES

LIST OF TABLES

ACRONYMS

NTR Negative Triangularity

PTR Positive Triangularity

ELMs Edge Localized Modes

MHD Magnetohydrodynamics

TCV Tokamak à configuration variable

RFX Reversed Field eXperiment

RFP Reverse Field Pinch

IK Internal Kink

XK External Kink

TM Tearing Mode

LCFS Last Closed Flux Surface

NBI Neutral Beam Injection

ECRH Electron Cyclotron Resonance Heating

SN Single Null

ITG Ion Temperature Gradient

NTM Neoclassical Tearing Mode

CHEASE Cubic Hermite Element Axisymmetric Static Equilibrium

MARS MAgnetohydrodynamic Resistive Spectrum

1

INTRODUCTION

The primary natural resources used to produce energy fall into three main categories: fossil fuels, nuclear fuels, and sunlight, which is the driver for most renewables. A common issue of all sources of energy is their efficiency of utilization, which directly impacts fuel reserves and/or cost.
Most of the world's energy, including electricity, is derived from fossil fuels, which produce greenhouse gases. If greenhouse gases emissions are to be curbed in the future in order to meet the commitments made by all the parties during the COP26 while coping with the energy demand increase, new energy capacity will have to be met by a combination of nuclear, hydroelectric, renewable sources.
The primary use of nuclear power is the large-scale generation of base load electricity by fission nuclear reactors. Notwithstanding the pubic concern about the use of nuclear energy, analyses and studies carried out since nuclear energy was established show that it is considerably safer than other energy sources and will likely be one of the main practical solutions for the future production of CO_2 free electricity.
Fusion is a form of nuclear energy. Its main application is the production of electricity in large base load power plants. The main advantages of fusion power are environmental impact and safety. Considering the environmental impact, fusion reactions produce no CO_2 or other greenhouse emissions. Also, they do not emit any other harmful chemicals into the atmosphere. The biggest environmental issue in the context of an hypothetical fusion reactor is that one byproduct is a high-energy neutron. However, these neutrons are captured in the blanket, hence they pose no threat to the public. Nonetheless, induced radioactivity can occur within the structural materials as neutrons pass through it on their way to the blanket; yet, this radioactive structural material has a short half-life so that the storage time required once it is removed is also short, on the order of 100 years, far less than the storage time required for long-lived nuclear waste. The potential advantages of fusion are indeed impressive from this point of view.

Thermonuclear fusion happens when a gas is sufficiently hot for the thermal motion of the nuclei to become so fast that they may overcome the repulsive Coulomb barrier and come close enough for the attractive nuclear forces to bring about the fusion reactions. This highly heated, ionized gas takes the name of *plasma*. A plasma is often presented as a completely ionized gas, consisting of freely moving positively charged ions, or nuclei, and negatively charged electrons. A more precise definition was given by Chen [1]: *a plasma is a quasi-neutral*

gas of charged and neutral particles which exhibits collective behavior. Fusion reactions involve light elements, mainly hydrogen (H) and its isotopes deuterium (D) and tritium (T); the last two are expected to be the main fuel for fusion reactors, due to the higher reaction rate at achievable temperatures.
Two methods of plasma confinement are currently being pursued: *magnetic* confinement and *inertial* confinement. The latter will not be considered in the present work. This thesis is set instead in the magnetic confinement framework, where a hot plasma is confined by means of external magnetic fields.

This thesis deals with some of the major issues connected to the achievement of a stable configuration for negative triangularity (NTR) tokamak plasmas, investigating the possible ideal kinks and instability modes through the use of computational codes. Over the span of around 30 years, the interest in this configuration raised considerably as a consequence of a modern reactors research line where not only the magnetic confinement but power exhaust and plasma stability as well are recognized as major issues. Experimental results seem to indicate that NTR plasmas keep L-mode edge characteristics for higher heating power with respect to positive triangularity (PTR) plasmas, leading to a significant mitigation of type-I ELMs bursts. Nevertheless, negative triangularity changes the plasma stability properties, which will be analyzed in this work.

Chapter 2

The MHD theory which describes the behavior of a plasma is briefly presented in Chapter 2.
In section 2.1 the MHD equilibrium equations are obtained. Section 2.2 is dedicated to the equilibrium theory for a tokamak configuration and to the description of the most important figures of merit for plasma equilibrium. Section 2.3 addresses the problem of linear stability. The different instabilities are finally discussed in section 2.4.

Chapter 3

Chapter 3 describes the features of negative triangularity plasmas. In section 3.1 a brief introduction to plasma confinement is provided, while section 3.2 exclusively focuses on NTR, featuring a summary of the experimental evidences obtained in the last three decades. Short presentations on the *Tokamak à configuration variable* (TCV) and on the RFX-mod machine conclude this chapter.

Chapter 4

In Chapter 4 the results of the analyses carried out on real plasma discharges of TCV and RFX-mod in tokamak configurations are presented and discussed. The analyses are performed by means of numerical codes for equilibrium solution (CHEASE) and linear resistive stability (MARS-F).
A summary of the work is provided in Chapter 5.
Appendices feature a broader description of the codes and the modeling framework used for the analyses, the workflows and the resistivity implementation in MARS-F.

2

MHD EQUILIBRIUM AND STABILITY

According to plasma physics textbooks, such as Goedbloed [2], a *fusion plasma* is a fully ionized gas where charged particles are subject to long range Coulomb interactions, this making the plasma a very good conductor. The needed amount of ionization, i.e. the ratio of ionized particles over the neutral ones, is described by the *Saha equation*, which gives an expression for the amount of ionization of a gas in thermal equilibrium:

$$\frac{n_i}{n_n} = \left(\frac{2\pi m_e k_B}{h^2}\right)^{3/2} \frac{T^{3/2}}{n_i} e^{-\frac{U_i}{k_B T}}$$

where m_e is the mass of an electron, h is the Planck's constant, k_B is Boltzmann's constant and U_i the ionization energy (typical value is $13.6eV$ for hydrogen). Considering typical values for those constants and hydrogen in a tokamak machine, with expected temperature $T \simeq 10^8$ K and densities $n = n_e = n_i \simeq 10^{20} m^{-3}$, one finds that $U_i \ll k_B T$, hence $e^{-\frac{U_i}{k_B T}} \simeq 1$ and $\frac{n_i}{n_n} \simeq 10^{13} \gg 1$. Thermonuclear fusion plasmas have typical densities and temperatures of respective order $n \sim 10^{20}\ \ m^{-3}$ and $T \sim 10keV = 116MK$.
The condition for controlled fusion reactions, instead, is expressed by the Lawson criterion, also referred to as *triple product*:

$$nT\tau \geq 3 \cdot 10^{21} m^{-3}\ s\ keV \quad (3.5 \cdot 10^{28} m^{-3}\ s\ K)$$

being $\tau = \tau_E$ the energy confinement time.

The reason for good plasma conductivity lies in its microscopic behavior: high temperature and low density cause Coulomb collisions to be very rare and thus resistance to be very low. However, describing plasma starting from a microscopic approach would require enormous efforts in both mathematical and computational terms.
The chapter is structured as follows: section 2.1 introduces the standard single-fluid model for the description of a plasma, namely the MHD model. An analysis of some of the terms appearing in the equations will also be provided. In section 2.2 the derivation of the Grad-Shafranov equation is illustrated. Finally, some figures of merit for plasma equilibrium description are discussed. Section 2.3 is devoted to the introduction of the stability theory applied to MHD equations, with a mathematical representation by means of the equation of motion involving the plasma displacement vector field, followed by a brief examination of another one by means of variational quadratic forms. Section 2.4 concludes this chapter with a discussion of the major plasma instabilities.

2.1 PLASMA DESCRIPTION

2.1.1 *MHD model*

Magneto-hydro-dynamics

In a sufficiently collisional plasma both electrons and ions move at the same average velocity and have the same temperature, and can therefore be treated as a single fluid. In other words, the separate identities of the ions and electrons do not appear. Equations 1, 2 and 3 are namely the mass conservation, total momentum and energy equation for a plasma

$$\frac{\partial \rho}{\partial t} + \vec{\nabla} \cdot (\rho \vec{v}) = 0 \tag{1}$$

$$\rho \left(\frac{\partial \vec{v}}{\partial t} + \vec{v} \cdot \vec{\nabla} \vec{v} \right) = \vec{j} \times \vec{B} - \vec{\nabla} p \tag{2}$$

$$\frac{D}{Dt} \left(\frac{p}{\rho^{\gamma}} \right) = 0 \quad where \quad \frac{D}{Dt} = \frac{\partial}{\partial t} + \vec{v} \cdot \vec{\nabla} \tag{3}$$

Due to the $\vec{j} \times \vec{B}$ term appearing in the system of PDEs, a coupling to the magnetic field becomes necessary. This coupling calls upon Maxwell's equations. The current density $\vec{j}$ is given, under the good hypothesis of small displacement current, by Ampère's law (equation 4), while the rate of change of $\vec{B}$ is given by Faraday's law (equation 5)

$$\mu_0 \vec{j} = \vec{\nabla} \times \vec{B} \tag{4}$$

$$\frac{\partial \vec{B}}{\partial t} = -\vec{\nabla} \times \vec{E} \tag{5}$$

It is now necessary to express the electric field in terms of the other variables. If the plasma is supposed to be perfectly conducting, in the local frame of the moving fluid no electric field can be sustained. This condition is expressed by the ideal Ohm's law

$$\vec{E} + \vec{v} \times \vec{B} = 0 \tag{6}$$

Equations 1-6, together with the solenoidal condition for $\vec{B}$, $\vec{\nabla} \cdot \vec{B} = 0$ constitute the *ideal MHD model*.
It is interesting to point out that, if the electric field is made explicit from equation 6 and plugged into equation 5, a relation between $\vec{B}$ and $\vec{v}$ is obtained

$$\frac{\partial \vec{B}}{\partial t} = \vec{\nabla} \times \left(\vec{v} \times \vec{B} \right) \tag{7}$$

This relation implies that the magnetic field lines move with the plasma velocity $\vec{v}$. Since plasma infinitesimal volume elements do not split into two (otherwise $\vec{v}$ would have to be discontinuous), a magnetic field line that moves with the plasma cannot be broken.

Resistive plasma

If instead the plasma is considered to be a non-perfect conductor with *resistivity* η, Ohm's law becomes

$$\vec{E} + \vec{v} \times \vec{B} = \eta \vec{j} \tag{8}$$

and substituting now equation 8 into equation 5, the obtained result is similar to the induction law 7, but with a new term due to resistivity appears

$$\frac{\partial \vec{B}}{\partial t} = \vec{\nabla} \times \left(\vec{v} \times \vec{B} \right) - \vec{\nabla} \times (\eta \vec{j}) \tag{9}$$

Equation 9 implies that the magnetic field lines again move with the plasma velocity but, in addition to this motion, the magnetic field changes in time due to a new term $\vec{\nabla} \times (\eta \vec{j})$. The tearing of a field line requires the tearing of a fluid element and this is not a physically allowable motion. It is for this reason that even a small resistivity can have a large impact on plasma stability. Resistivity allows magnetic field lines to *diffuse* through the plasma so that the frozen-in topological constraint expressed by equation 7 is removed. A measure of the *diffusivity* of the plasma can be obtained by substituting Ampère's law 4 into equation 9

$$\frac{\partial \vec{B}}{\partial t} = \vec{\nabla} \times \left(\vec{v} \times \vec{B} \right) - \vec{\nabla} \times \left(\eta \frac{1}{\mu_0} \vec{\nabla} \times \vec{B} \right) \tag{10}$$

Considering the relation

$$\vec{\nabla} \times \left(\frac{\eta}{\mu_0} \vec{\nabla} \times \vec{B} \right) = \frac{\eta}{\mu_0} \vec{\nabla} \left(\vec{\nabla} \cdot \vec{B} \right) - \frac{\eta}{\mu_0} \nabla^2 \vec{B} = -\frac{\eta}{\mu_0} \nabla^2 \vec{B}$$

under the hypothesis of uniform $\frac{\eta}{\mu_0}$ and exploiting the fact that the magnetic field is solenoidal. It is therefore possible to rewrite the above equation, defining the *magnetic diffusivity* $D_\eta = \eta / \mu_0 [m^2/s]$, as

$$\frac{\partial \vec{B}}{\partial t} = \vec{\nabla} \times \left(\vec{v} \times \vec{B} \right) + D_\eta \nabla^2 \vec{B} \tag{11}$$

It is clear from equation 11 that the magnetic field moves with velocity equal to the plasma velocity $\vec{v}$, and it diffuses with a diffusion coefficient D_η. The fact that the magnetic field diffuses implies that magnetic field lines can be broken. In general, the resistive form of Ohm's law is only needed in regions of high current concentration, which are usually extremely thin. Still, such current sheets do actually occur and play an important role in models for the aforementioned disruptive phenomena.

2.1.2 *Spitzer's resistivity model and Lundquist number*

More accurate calculations involving kinetic plasma models, as discussed in [3], show that the actual resistive Ohm's law is of the form

$$\vec{E} + \vec{v} \times \vec{B} = \eta_{\parallel} \vec{j}_{\parallel} + \eta_{\perp} \vec{j}_{\perp}$$

where subscripts $\parallel$ and $\perp$ refer to the directions parallel and perpendicular to the magnetic field.
The resistivity is therefore anisotropic, and the more accurate value of the parallel resistivity is reduced by a factor of about 1/2: $\eta_{\parallel} = 0.51\eta$.
Spitzer [4] discussed the formula for the resistivity coming from classical models

$$\eta = \frac{m_e \nu}{n_e e^2}$$

since in a fully ionized gas there is some uncertainty as to the appropriate value of ν to use. A rough estimate is obtained by using $\nu = \nu_e$ electron collision frequency. Spitzer et al. [4] [5] found that, for singly charged ions, the resistivity is well described by the formula

Spitzer resistivity

$$\eta_{\parallel} = 0.51 \frac{e^2 m_e^{1/2} \ln \Lambda}{3\varepsilon_0^2 (2\pi)^{3/2}} T_e^{-3/2} = 1.65 \cdot 10^{-9} \ln \Lambda \, T_e^{-3/2} \Omega m \quad T_e \; in \; keV \tag{12}$$

They also found a relation between the perpendicular and the parallel resistivity

$$\eta_{\parallel} = \eta_{\perp} F(Z)$$

For Z=1, for example, it is found that $\eta_{\parallel} = \eta_{\perp}/1.96$.
Equation 12 can be generalized: for a collisional plasma composed of a single specie of ions of charge Z, the plasma resistivity is approximately given by the formula

$$\eta_{\parallel}(Z) = N(Z) Z \eta_{\parallel}(1) \tag{13}$$

where $\eta_{\parallel}(1)$ is the resistivity given by equation 12. Calculations of values of $N(Z)$ were carried out by Spitzer and Härm and are tabulated [5]. Thus, the resistivity decreases with temperature $\eta \sim 1/T^{3/2}$ as the plasma is heated, implying a corresponding decrease in heating efficiency. Resistivity allows a wider range of possible instabilities than ideal MHD. However, these instabilities have much slower growth rates and usually do not lead to a macroscopic loss of plasma, but instead to enhanced transport losses. Furthermore, even in the absence of resistive instabilities, resistivity still represents the only dissipation term in the momentum equation. This dissipation gives rise to particle diffusion and magnetic field diffusion, representing two main transport losses. Here too, the phenomena occur on much slower time scales than the characteristic MHD time scale.

It is possible to characterize the strength of the resistive term using the characteristic time of the magnetic field diffusion

$$\tau_\eta = \frac{L^2}{\eta}$$

where L is the characteristic length of the system.
The importance of the resistivity in the plasma is measured by comparing this characteristic time with the Alfvén time

$$\tau_A = \frac{L}{v_A}$$

where

$$v_A = \frac{B}{\sqrt{\rho\mu_0}}$$

This comparison gives the *Lundquist number* S, which is a particular case of the *magnetic Reynols number* when the typical velocity scale of the system is the Alfvén velocity v_A *Lundquist number*

$$S = \frac{\tau_\eta}{\tau_A} = \frac{BL}{\eta}\sqrt{\frac{\mu_0}{\rho}} \tag{14}$$

In this work the effect of the variation of Lundquist number (therefore the variation of the resistivity) on plasma stability will be considered.

2.2 TOKAMAK CONFIGURATION EQUILIBRIUM

2.2.1 *The Grad-Shafranov equation*

Up to now, no hypotheses were made about the geometry where the MHD equations should be solved. For the purposes of this work, the set of coordinates which will be considered is the toroidal one for a tokamak machine: being R the major radius, ϕ the toroidal angle and Z the vertical coordinate, in order to have a right-handed coordinate system rotating counterclockwise, the set has to be (R, ϕ, Z). Given such coordinates, the magnetic field $\vec{B}$ can be written as:

$$\vec{B} = B_\phi \hat{e}_\phi + \vec{B}_p = B_\phi \hat{e}_\phi + B_R \hat{e}_R + B_Z \hat{e}_Z$$

where $\vec{B}_p$ is the poloidal field, lying on the (R, Z) plane.

When dealing with a **static**, **axisymmetric** equilibrium, that is an equilibrium presenting no variation in time and independent upon the toroidal angle ϕ, the requirements are:

$$\frac{\partial *}{\partial t} = \frac{\partial *}{\partial \phi} = 0 \qquad\qquad \vec{v} = 0$$

therefore, equations 1-3 reduce to

$$\vec{j} \times \vec{B} = \vec{\nabla} p \tag{15}$$

which is the fundamental condition for a tokamak equilibrium: there must be internal balance between the pressure of the plasma and the forces due to the magnetic field. In an axisymmetric equilibrium, the magnetic surfaces will form a set of nested toroids rotating around the center of the tokamak, as shown in figure 1.

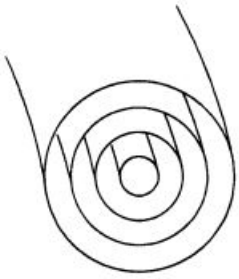

Figure 1: Magnetic surfaces forming nested toroids [5].

In order to study such a configuration, it is useful to introduce the **poloidal flux function** ψ within each magnetic surface. This function is constant on a given magnetic surface, and is defined as

$$\psi = \int \vec{B}_p \cdot d\vec{S}_\psi \tag{16}$$

The definition of the poloidal surface element over which the integral is carried out is presented in figure 2. The poloidal flux function here defined is associated with a unit angle in ϕ. In some books its definition is slightly different, such as in Freidberg's book [6], and it is simply larger by a factor 2π.
From this definition it follows that, in a toroidal coordinate system

$$B_R = -\frac{1}{R}\frac{\partial \psi}{\partial Z}$$

$$B_Z = \frac{1}{R}\frac{\partial \psi}{\partial R}$$

In this sense, the poloidal flux acts as a stream function for the poloidal magnetic field. In a more compact notation, it is possible to write

$$\vec{B}_p = \frac{1}{R}\vec{\nabla}\psi \times \hat{e}_\phi \tag{17}$$

The very same can be done for the current density $\vec{j}$, defining a **current flux function** f and obtaining the relation

$$\vec{j}_p = \frac{1}{R}\vec{\nabla} f \times \hat{e}_\phi \tag{18}$$

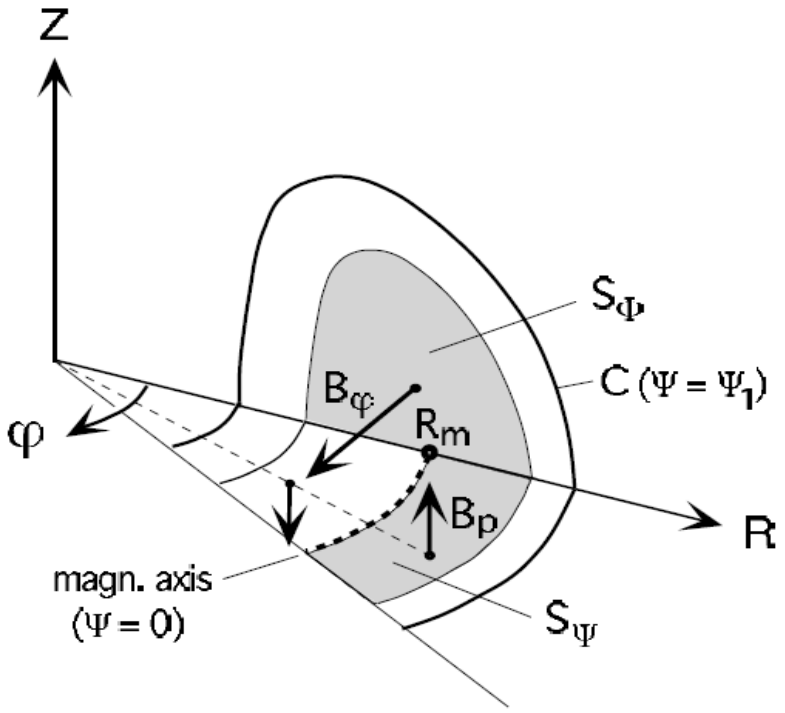

Figure 2: Poloidal and toroidal surface elements dS_ψ and dS_ϕ [2].

For a static, axisymmetric equilibrium, an expression for f using Ampère's law can be provided

$$\vec{\nabla} \times \vec{B} = \mu_0 \vec{j} \Longrightarrow \begin{cases} j_R = -\frac{1}{\mu_0} \frac{\partial B_\phi}{\partial Z} \\ j_Z = \frac{1}{\mu_0} \frac{1}{R} \frac{\partial (R B_\phi)}{\partial R} \end{cases} \tag{19}$$

and the only way to let those quantities be equal to 18 is setting

$$f = \frac{R B_\phi}{\mu_0} \tag{20}$$

Now the expressions for $\vec{B}$ and $\vec{j}$ can be substituted in the momentum equation 2. Before doing that, an interesting step to carry out is decomposing equation 2 into two components along $\vec{B}$ and $\vec{j}$. Considering the projection on $\vec{B}$, and recalling that $\vec{j} \times \vec{B}$ is a quantity orthogonal to both $\vec{j}$ and $\vec{B}$

$$\vec{B} \cdot \vec{j} \times \vec{B} = \vec{B} \cdot \vec{\nabla} p \Longrightarrow \vec{B} \cdot \vec{\nabla} p = 0$$

which can be rewritten, using equation 17, as

$$\hat{e}_\phi \cdot \vec{\nabla} \psi \times \vec{\nabla} p = 0 \tag{21}$$

Equation 21 has the general solution

$$p = p(\psi) \tag{22}$$

Thus, there is no pressure gradient along the magnetic field lines, and the magnetic surfaces are surfaces of constant pressure. It is important to notice that the use of ψ leads to having the pressure dependent upon a single variable, even though the geometry is two dimensional.
The same considerations can be made for $\vec{j}$, showing that the pressure is constant not only on the magnetic surfaces but also along the current lines

$$\vec{j}\cdot\vec{j}\times\vec{B} = \vec{j}\cdot\vec{\nabla}p \Longrightarrow \vec{j}\cdot\vec{\nabla}p = 0$$

which can be rewritten, using equation 18, as

$$\hat{e}_\phi\cdot\vec{\nabla}\psi\times\vec{\nabla}\left(\frac{RB_\phi}{\mu_0}\right) = \hat{e}_\phi\cdot\vec{\nabla}\psi\times\vec{\nabla}f = 0 \tag{23}$$

hence, equation 23 shows that f is a free function too, depending only on ψ

$$f = f(\psi) \tag{24}$$

Equation 2 can be rewritten as

$$\vec{j}_p\times\hat{e}_\phi B_\phi + \jmath_\phi\hat{e}_\phi\times\vec{B}_p = \vec{\nabla}p \tag{25}$$

and substituting equations 17 and 18 into 25

$$\vec{\nabla}p = -\frac{B_\phi}{R}\vec{\nabla}f + \frac{\jmath_\phi}{R}\vec{\nabla}\psi \tag{26}$$

Using now the results obtained from equations 22 and 24, it is possible to write an equation where the only unknowns are $\jmath_\phi$ and ψ.
First of all, due to the previous results, it is possible to write

$$\vec{\nabla}f(\psi) = \frac{df}{d\psi}\vec{\nabla}\psi \qquad\qquad \vec{\nabla}p(\psi) = \frac{dp}{d\psi}\vec{\nabla}\psi$$

From equation 20 an expression for B_ϕ can be obtained

$$B_\phi = f\frac{\mu_0}{R} \tag{27}$$

and $\jmath_\phi$ is made explicit from equation 26

$$\jmath_\phi = R\frac{dp}{d\psi} + \frac{\mu_0}{R}f\frac{df}{d\psi} \tag{28}$$

The final step consists in exploiting the previously neglected last component of Ampère's law, in equation 19

$$\mu_0\jmath_\phi = \frac{\partial B_R}{\partial Z} - \frac{\partial B_Z}{\partial R} = -\frac{1}{R}\frac{\partial^2\psi}{\partial Z^2} - \frac{\partial}{\partial R}\left(\frac{1}{R}\frac{\partial\psi}{\partial R}\right) \tag{29}$$

Finally, the combination of equations 29 and 28 (changing signs and multiplying by μ_0 and R) provides the Grad-Shafranov equation

$$R\frac{\partial}{\partial R}\left(\frac{1}{R}\frac{\partial \psi}{\partial R}\right)+\frac{\partial^2 \psi}{\partial Z^2}=-\mu_0 R^2\frac{dp}{d\psi}-{\mu_0}^2 f(\psi)\frac{df}{d\psi} \tag{30}$$

or in an alternative form

$$R\frac{\partial}{\partial R}\left(\frac{1}{R}\frac{\partial \psi}{\partial R}\right)+\frac{\partial^2 \psi}{\partial Z^2}=-\mu_0 R^2 p'(\psi)-{\mu_0}^2 f(\psi)f'(\psi) \tag{31}$$

Equation 30 is typically solved by means of numerical codes. An example of output of such codes is shown in figure 3: the aforementioned nested toroids formed by magnetic surfaces are found to be level surfaces of the solutions of the Grad- Shafranov equation.

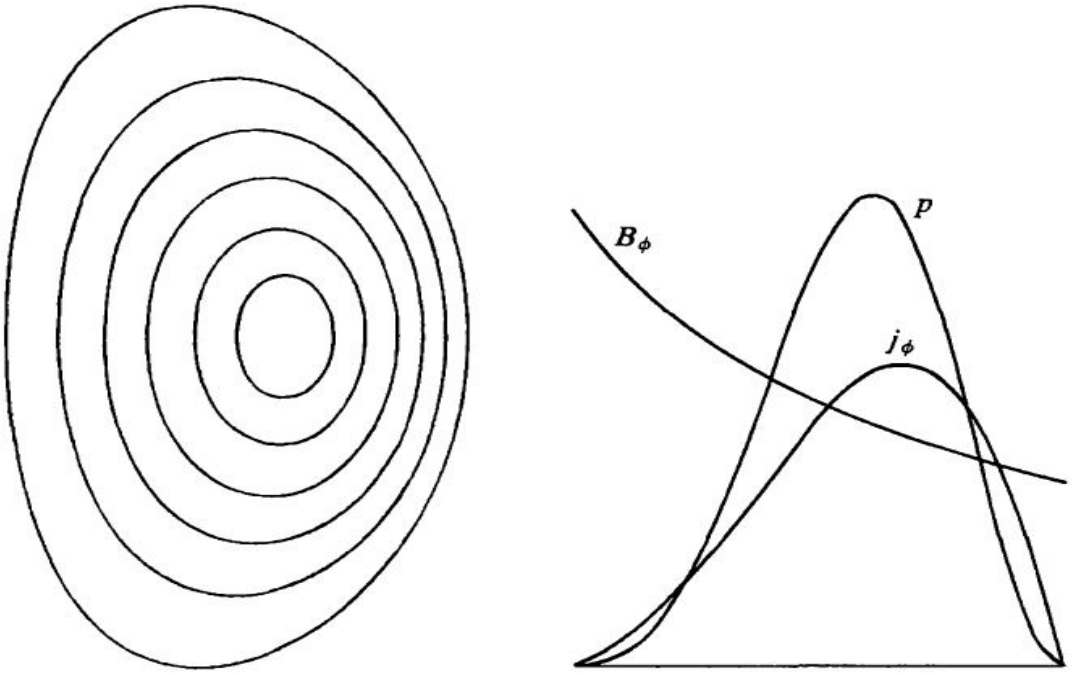

Figure 3: Profiles for toroidal field, pressure and current obtained by solving the Grad-Shafranov equation (on the right). The magnetic surfaces show the typical *D-shape* (on the left) [5].

2.2.2 *Figures of merit for plasma description*

Among the different figures of merit for a fusion relevant plasma, two stand out. The first one is the *safety factor q*. Its values, especially the rational ones, play a role in determining plasma stability. Its values represent a physical behavior of the magnetic field lines, namely the variation in angle $\Delta\phi$ required to the field line to return to its starting position on the poloidal plane

$$q = \frac{\Delta\phi}{2\pi}$$

For a large aspect ratio tokamak with circular cross section, a good approximation for the safety factor is

$$q = \frac{rB_\phi}{RB_p}$$

where r is the minor radius of the given flux surface which q is evaluated at. From this relation, it is clear that q will present its minimum at, or close to, the magnetic axis, and increasing while moving outward. For plasmas which present a limiter, the former relation persists for non-circular plasmas [5]. Nonetheless, precise values can be evaluated by numerical solution of the equilibrium. Otherwise, should the plasma present a separatrix or divertor configuration, the q profile is modified, due to the contributions close to the X-point.

The second fundamental parameter that ought to be mentioned is the β factor. Defined as the ratio of kinetic to magnetic pressure

$$\beta = \frac{p}{B^2/2\mu_0},$$

it evaluates the efficiency of confinement of plasma pressure by the magnetic field. The achievable value of β is often limited by plasma instabilities. Different betas are used to describe a reactor plasma; among them the two most utilized are the *toroidal beta* β_T, defined as the ratio of the kinetic pressure to the toroidal magnetic field pressure:

$$\beta_T = \frac{\langle p \rangle}{B_\phi^2/2\mu_0}$$

and the normalized beta β_N obtained by normalizing β_T with respect to the plasma current itself (B_ϕ being the toroidal magnetic field):

$$\beta_N = \beta_T \frac{aB_\phi}{I}$$

2.3 MHD STABILITY

2.3.1 *Ideal MHD stability*

MHD stability

The idea behind linear stability is to study the behavior of a dynamic system (in this case: the plasma) with respect to **small** (i.e. infinitesimal) perturbations. Considering a generic quantity A (it might be a scalar or a vector quantity), it can be linearized around its equilibrium value [6]

$$A = A(\vec{r}, t) = A_0(\vec{r}) + A_1(\vec{r}, t) \tag{32}$$

with the main assumption

$$\frac{\|A_1\|}{\|A_0\|} \ll 1 \tag{33}$$

It is fundamental to notice that, while the equilibrium value depends only on space, the perturbed quantity also depends upon time.
With this idea, all the quantities figuring in the ideal MHD equations are linearized. The only quantity which presents a slightly different linearized form from the others is the velocity: since its equilibrium value is zero (hp. static equilibrium), its linearized form is simply

$$\vec{v}(\vec{r}, t) = \vec{v}_1(\vec{r}, t) \tag{34}$$

By substitution in the MHD set of equations (mass, momentum, energy and Maxwell's), the linearized set can be obtained.
As an example, the momentum equation would have the following form

$$(\rho_0 + \rho_1)\left(\frac{\partial \vec{v}_1}{\partial t} + \vec{v}_1 \cdot \vec{\nabla}\vec{v}_1\right) = (\vec{j}_0 + \vec{j}_1) \times (\vec{B}_0 + \vec{B}_1) - \vec{\nabla}(p_0 + p_1) \tag{35}$$

From this one, performing multiplications and retaining only the first order terms

$$\rho_0 \frac{\partial \vec{v}_1}{\partial t} = \vec{j}_1 \times \vec{B}_0 + \vec{j}_0 \times \vec{B}_1 - \vec{\nabla} p_1 \tag{36}$$

To avoid the issue of the time integration, a lagrangian displacement vector $\vec{\xi}(\vec{r}, t)$ of a plasma element from its equilibrium position can be introduced. The fluid velocity $\vec{v}(\vec{r}, t)$ then becomes the lagrangian derivative of the displacement

$$\vec{v} = \frac{\partial \vec{\xi}}{\partial t} + \vec{v} \cdot \vec{\nabla}\vec{\xi} \approx \vec{v}_1 = \frac{\partial \vec{\xi}}{\partial t} \Longrightarrow \frac{\partial \vec{v}_1}{\partial t} = \frac{\partial^2 \vec{\xi}}{\partial t^2} \tag{37}$$

since the $\vec{\nabla}\vec{\xi}$ term is a second order one.
By exploiting the displacement quantity in the linearized MHD equations, after

time integration and after making the quantities p_1, ρ_1, $\vec{B}_1$, $\vec{j}_1$ explicit, a useful expression of the momentum equation can be obtained

$$\rho_0 \frac{\partial^2 \vec{\xi}}{\partial t^2} = \vec{\nabla}(\vec{\xi} \cdot \vec{\nabla} p_0 + \Gamma p_0 \vec{\nabla} \cdot \vec{\xi}) + \vec{j}_0 \times [\vec{\nabla} \times (\vec{\xi} \times \vec{B}_0)] + \frac{1}{\mu_0} \vec{\nabla} \times [\vec{\nabla} \times (\vec{\xi} \times \vec{B}_0)] \times \vec{B}_0 \tag{38}$$

or, in a more compact form

$$\rho_0 \frac{\partial^2 \vec{\xi}}{\partial t^2} = F(\vec{\xi}) \tag{39}$$

The term $F(\vec{\xi})$ is called **force operator**; Γ is the adiabatic index.
The quantity $\vec{\nabla} \times (\vec{\xi} \times \vec{B}_0)$ is the perturbed field $\vec{B}_1$, and $\vec{j}_0$ can be written, from Ampère's law, as $\vec{\nabla} \times \vec{B}_0$. Those redefinitions lead to an alternative form of the force operator

$$F(\vec{\xi}) = \vec{\nabla}(\vec{\xi} \cdot \vec{\nabla} p_0 + \Gamma p_0 \vec{\nabla} \cdot \vec{\xi}) + (\vec{\nabla} \times \vec{B}_0) \times \vec{B}_1 + \frac{1}{\mu_0} (\vec{\nabla} \times \vec{B}_1) \times \vec{B}_0 \tag{40}$$

In equation 38, each one of the terms of the force operator has a physical meaning

- $\vec{\nabla}(\vec{\xi} \cdot \vec{\nabla} p_0)$ represents a force due to the equilibrium pressure gradient; this may cause instabilities;
- $\vec{\nabla}(\Gamma p_0 \vec{\nabla} \cdot \vec{\xi})$ represents an isotropic force due to the plasma compressibility; it is associated with stable plasma perturbations;
- $\vec{j}_0 \times \vec{B}_1$ represents a force due to the equilibrium current; this term may also lead to instabilities;
- $\frac{1}{\mu_0}(\vec{\nabla} \times \vec{B}_1) \times \vec{B}_0 = -\frac{1}{\mu_0} \vec{B}_0 \times (\vec{\nabla} \times \vec{B}_1)$ represents a force orthogonal to $\vec{B}$, due to field line bending.

2.3.2 *Normal modes*

Separating the variable for the quantity $\vec{\xi}$ and writing the solution in the form of **normal modes**

$$\vec{\xi}(\vec{r}, t) = \hat{\xi}(\vec{r}) e^{-i\lambda t} \tag{41}$$

where $\lambda = \gamma + i\omega$.This leads to the following form of equation 39

$$\rho_0 \frac{\partial^2 \vec{\xi}}{\partial t^2} = -\rho_0 \lambda^2 \hat{\xi} = F(\hat{\xi}) \tag{42}$$

Eigenvalue problem

Equation 42 represents the stability problem as an **eigenvalue problem**. In general, the eigenvalue λ is a complex quantity. A property of the force operator is its self-adjointness for ideal MHD; as a consequence, the eigenvalues λ^2 are forced to be purely real. Hence, considering only its real part γ:

- if $\gamma^2 > 0$ then the perturbations are stable oscillations;
- if $\gamma^2 < 0$ then γ is purely imaginary; it follows that the argument of the exponential becomes real and leads to an exponential growth; therefore it is unstable.

2.4 PLASMA INSTABILITIES

The strongest tokamak instabilities arise from [5]:

- $\vec{\nabla} p$ (pressure gradients)
- current gradients (in particular, the radial gradient of the equilibrium toroidal current density)

The resulting instabilities are divided in:

- *ideal modes*: this implies that instabilities can arise even if the plasma were perfectly conducting (i.e. plasma resistivity $\eta = 0$)
- *resistive modes*, due to finite resistivity of the plasma

In genera, both ideal and resistive instabilities might present an infinite spectrum of modes, each one characterized by its toroidal and poloidal mode numbers n, m. Conversely, considering a discrete set of modes, in the case of a circular, large aspect-ratio tokamak, these modes take the form $e^{-i(n\phi - m\theta)}$. The resonant surfaces, for which the stability presents a minimum, are the ones on which $m = nq$, q being the safety factor. For low mode numbers, the modes are not localized [5], while for $m, n \to \infty$ the modes are localized enough to consider stability a magnetic surface property.

The macroscopic deformations which often appear in tokamaks are:

1. *external kink* (XK): it is an ideal instability which is in general current-driven at low-β, while in tokamaks at high-β also pressure gradients can contribute to this instability. The XK acts on the LCFS, modifying its shape and possibly leading to disruptions
2. *internal kink* (IK): it is a current-driven instability with mode number $m = 1$ which affects the plasma if the minimum value of the safety factor is less than unity ($q_{min} < 1$). Also the pressure can have an effect on the IK [7]. An internal kink leads to an alteration of the eigenfunction which remains inside the confined plasma, therefore acting on the core of the plasma while not modifying the last closed flux surface.

3. *tearing mode* (TM): a tearing modes is an instability related to the formation and development of magnetic islands. Experimentally, these modes can be stabilized with increasing pressure in tokamak configurations, as it will be discussed later

Wesson [5] proposed a shape of the current density of the form

$$\jmath = \jmath_0 \left(1 - (r/a)^2\right)^{\nu}$$

by which it is possible to obtain a class of analytical results for a large aspect-ratio device with circular plasma cross section. By exploiting this current profile it is possible to evaluate the ratio $q(r = a)/q_0 = \nu + 1$ (a being the plasma radius). Internal kinks are characterized by the resonant surface $q = 1$, thus these instabilities arise only if that resonant surface is present. Consequently, the requested $q > 1$ is a sufficient condition for stability of the IK. The stability diagram of kink modes with internal kinks is presented in figure 4. In particular, for the aforementioned current shape, requesting $q > 1$ is the same as requesting $q_0 > 1$, where q_0 is the value of the safety factor at the magnetic axis. This request is almost confirmed by experiments, where the minimum value of the safety factor profile q_{min} occurs close to the magnetic axis, and the difference between q_{min} and q_0 is relatively small.

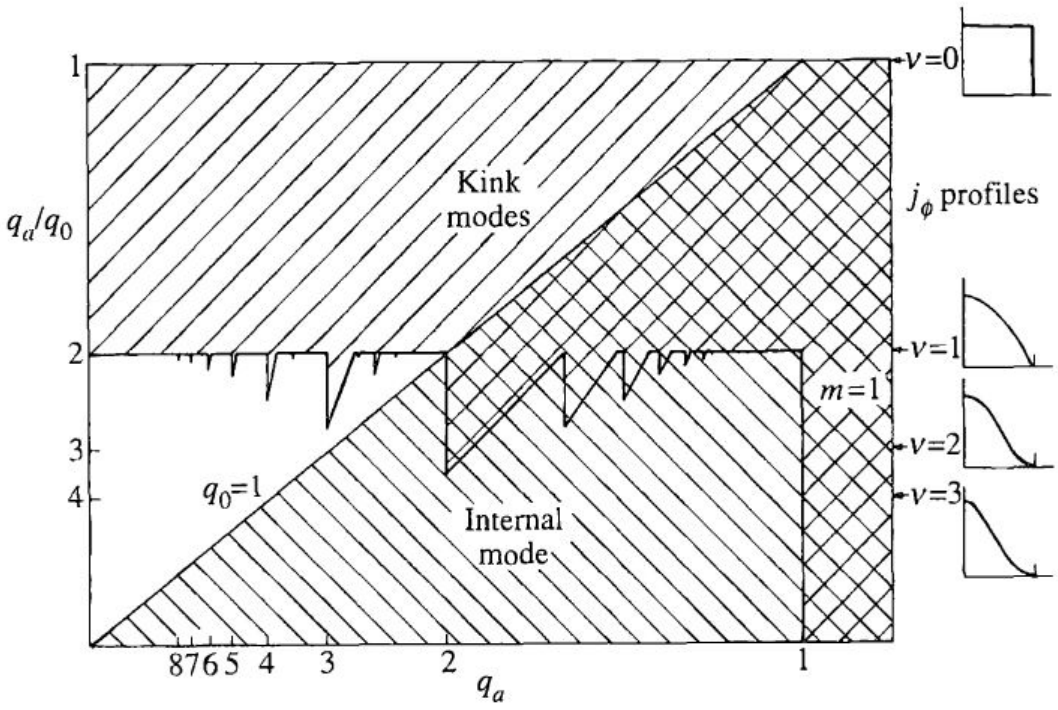

Figure 4: Stability diagram for kink modes, with internal kinks [5].

Potentially, kink modes are the strongest instabilities, leading to the kinking of the magnetic surfaces and of the plasma boundary. The so-called *external*

kink (XK) proves to be a major issue in achieving proper fusion plasmas. More precisely the XK is an obstacle to the high β_T values desired for fusion purposes. As far as the tokamak configuration is concerned, both the aforementioned law and the Troyon scaling law are found to be valid. This criterion introduces a limit on the maximum achievable β to prevent the onset of a pressure driven instability. Troyon's law states that the maximum β_T scales as the total plasma current:

Troyon scaling law

$$\beta_N^{Troyon} = 2.8 \tag{43}$$

Boundary condition of no external resistive wall is taken. Nonetheless, it was noticed that two parameters, elongation and triangularity, can strongly affect the Troyon limit for D-shaped plasmas [8]. Any resistive wall surrounding the plasma would have no effect on stability thresholds. In fact it has been proven that the resistivity of the external wall does not stabilize the external kink but only reduces its growth rate by a factor of the order of ${\tau_W}^{-1}$, where τ_W is the flux diffusion time scale through the wall.
Tearing modes are driven by the radial gradient of the equilibrium toroidal current density: these modes lead to a tearing and a consequent rejoining of the magnetic field lines, which are a consequence of the finite resistivity of the plasma. Figure 5 shows a stability regime diagram for a circular, straight tokamak. In this scheme, tearing and kink modes are compared considering the aforementioned current density shape for both.

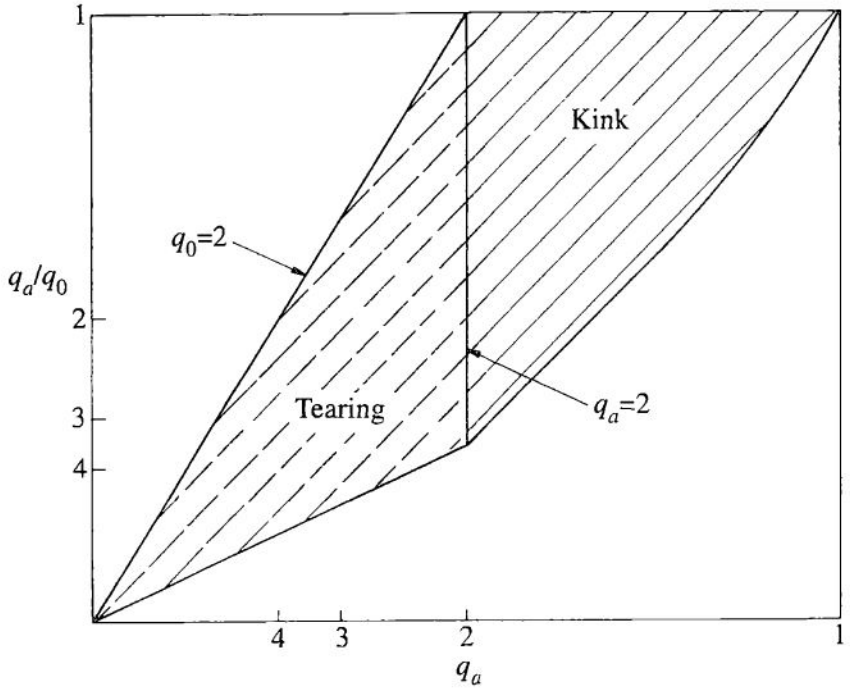

Figure 5: Stability diagram for $m = 2$ tearing and kink modes for a circular tokamak [5].

The toroidal curvature effects, which are not taken into account in the stability regime of figure 5, have a strong influence on the stability of resistive modes, due to the fact that the resistivity is small. Also the pressure effect is not considered, while in real plasmas it contributes to the stability of TM: Glasser et al. [9] and Bondeson et al. [10] showed either analytically and numerically that the tearing mode is stabilized by favourable average curvature when β and $S = 1/\eta$ are sufficiently large.

The next chapter features a series of selected works regarding the comparison of negative and positive triangularity plasmas, in order to sustain the advantages of NTR plasma shape from different points of view, in the light of reactor-relevant plasmas.

3

NEGATIVE TRIANGULARITY PLASMAS

3.1 BRIEF INTRODUCTION TO PLASMA CONFINEMENT

Qualitatively, two distinct modes of operation for tokamak experiments are feasible. These are, namely, the *L-mode*, referring to lower grade confinement, and the *H-mode* [11], referring to higher grade confinement. Practically, the energy confinement time τ_E for the H-mode is about a factor of 2 higher than the one of L-mode.
The amount of external heating power supplied and the way in which the plasma makes contact with the first material surface shall be investigated thoroughly, in order to determine which operation regime prevails. The reason for the L-to-H transition has not yet been fully understood on a physical level. The prevailing belief is that at high auxiliary power levels strongly sheared flow velocities develop near the plasma edge that act to stabilize micro-turbulence. However, the theories are far from complete.
In terms of contact of the plasma with the first material surface, it is possible to use two concepts for the plasma-wall interface, known as the limiter and the divertor. The idea behind the limiter is that as the plasma slowly diffuses across the last closed flux surface (LCFS), both particles and energy are rapidly deposited on the limiter surface due to the enormously higher parallel transport, while simultaneously isolating the first wall from the plasma. The limiter has the advantage of a simpler, more compact construction, though its close proximity to the plasma almost always increases the number of impurities diffusing into the plasma.

Limiter

Conversely, the divertor is more efficient in isolating the plasma from impurities due to its remote location, but tends to focus the heat load onto a narrow area of the target plates. Plasma experimentalists believe that impurity isolation is the dominant issue. Nonetheless, a combination of high external power and divertor geometry is desirable for accessing H-mode operation [3].

Divertor

H-mode profiles typically develop pedestals in the edge density and edge temperature, resulting in an increase in the edge pressure. The narrow transition layer between the plasma edge and the actual first material surface thus has the appearance of an edge pedestal in pressure. The ability of the plasma to support a substantial edge pressure suggests the formation of an edge "transport barrier" that prevents the rapid loss of energy. This transport barrier leads to an increase in the average density and a higher central temperature, both of which correspond to an improvement in the energy confinement time τ_E. However,

H-mode operation also has some potential disadvantages. If the buildup of edge density goes unchecked, eventually the Greenwald density limit [12]

$$n_G[10^{20}m^{-3}] \leq \frac{I_p[MA]}{\pi a^2[m^2]}$$

may be violated, leading to a disruption.
Before this limit is reached, localized edge instabilities are excited inside the plasma. These are known as ELMs (Edge Localized Modes), driven by the large edge pressure and current gradients associated with H-mode operation. When the edge pressure gradient becomes too high a burst of ELMs is triggered, thereby relieving the excess pressure, reducing plasma density and temperature in the outer zone (in ITER, the energy lost in this process is expected to reach peaks of $\sim 21MJ$, leading to scaled amplitudes not acceptable in the future DEMO reactor). Such an energy reduction, together with temperature fall, leads to a reduction of the H-mode transport barrier.

The situation is further complicated by the fact that there are different types of ELMs whose positive and negative contributions to tokamak operation might vary. For example, type-I ELMs are short in duration, well-spaced in time but very intense in magnitude. This is clearly shown in figure 6.

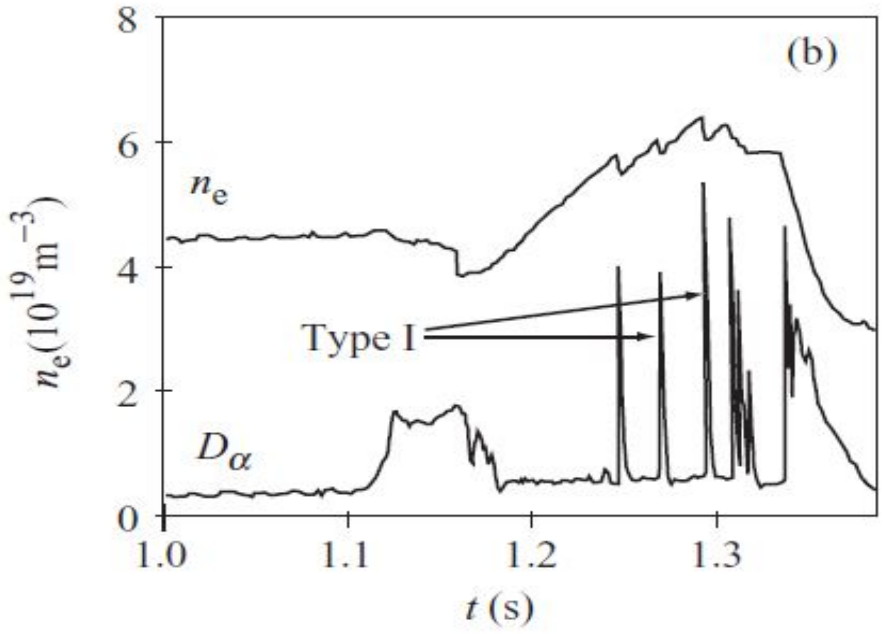

Figure 6: D_α radiation emission showing type-I ELM activity during H-mode operation with NBI in ASDEX [11] (Picture taken from [5]).

3.2 OVERVIEW OF EXPERIMENTAL RESULTS

3.2.1 *Effects of triangularity on energy confinement time*

H-mode negative triangularity plasmas present lower edge stability thresholds, with a rising increased frequency of type-I ELMs. However, experiments indicate the possibility to keep L-mode edge confinement characteristics in negative triangularity configuration with heating power higher than the one required in positive triangularity; nevertheless plasma properties are drastically changed in such a configuration. More precisely, shape and confinement mode have been noticed to influence the transport properties of the plasma. In particular the plasma shape is characterized by two parameters, namely *elongation* κ and *triangularity* δ. These two influence the energy confinement time both for L- and H-mode. This is well described for a ohmically heated, L-mode plasma by the empirical law ITER89-P [13]:

Plasma properties

$$\tau_E^{ITER89-P} \propto \kappa^{0.5} \tag{44}$$

A slightly modified scaling law for L-mode discharges was proposed by ITER research group [14]:

$$\tau_E^{ITER-98-L} \propto \kappa^{0.64} \tag{45}$$

Still, both formulae consider the energy confinement time to be independent on the triangularity. A study carried out by Moret et al. [15] showed that for an ohmic, L-mode plasma the energy confinement time (quantified in this study by the *electron* energy confinement time τ_{E_e}) improves slightly with elongation and strongly degrades for positive triangularities. An eventual plasma current dependence was removed through current scans. Furthermore, internal sawtooth disruptions were noticed to be larger at positive triangularities and almost vanishing at negative ones.

Nonetheless, the ohmic heating is not the only (neither the most favored) heating method. Different studies focused on the influence of plasma shape on τ_E were carried out for electron cyclotron heating (ECH), eventually coupled with neutral beam injection (NBI). In these studies, the TCV tokamak features were exploited, seeing as it is capable to operate with edge elongation $0.9 < \kappa < 2.8$ and edge triangularity $-0.7 < \delta < 1$ [16] [17]. The main result obtained is that, when the plasma is not purely ohmically heated, but a considerable fraction of power is provided by ECH/NBI, its energy confinement time is dependent on triangularity.

Not-purely ohmic plasmas

Experimental evidences led to a scaling law for plasma current of the form $I_p \propto (\kappa^2 + 1)/2$. Thus, the interest in highly elongated plasma raised due to the fact that energy confinement time is usually linearly proportional to plasma

current; also, a vertically elongated plasma allows higher values of β, hence higher values of plasma pressure [18]. For a fixed elongation of $\kappa = 1.5$ in a plasma where the ECH exceeded the ohmic heating by up to one order of magnitude, τ_{E_e} was noticed to decrease with power and triangularity [19] as:

$$\tau_{E_e} \propto I_p^{\alpha_I} \kappa^{1.4(1-\alpha_I)} (1+\delta)^{-0.35} \tag{46}$$

This relation is compared to ITER-98-L (equation 45) in figure 7. The beneficial effect of negative triangularity is evident. Moreover, Camenen et al. [20] noticed that electron heat transport was halved at negative triangularities with respect to positive ones for comparable plasma conditions, as shown in figure 8. Furthermore, negative triangularity tokamaks can be capable of doubling the energy confinement time in TEM (trapped electron modes)-dominated, L-mode regime.

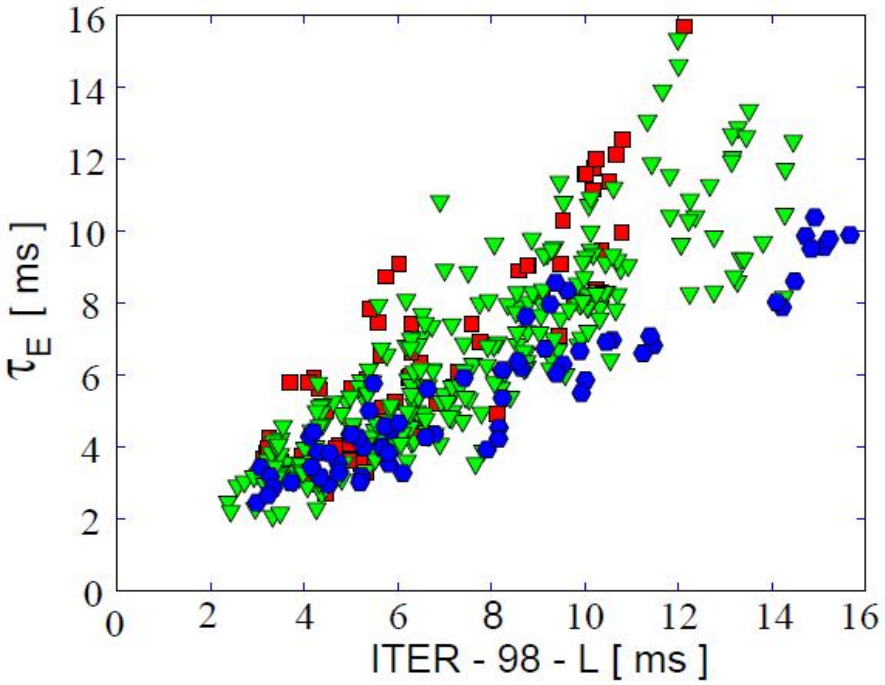

Figure 7: Fit to the ITER-98-L (equation 45) mode scaling law of TCV experimental results. Since triangularity does not appear in ITER-98-L, it is explicitly indicated by the symbols: red squares, $\delta < 0$; green triangles, $0 < \delta < 0.3$; blue hexagons, $\delta > 0.3$). Negative delta appears favourable [19].

For ohmic plasmas, the collisionality is higher and independent from triangularity, while it diminishes when the plasma is heated with electron cyclotron and decreases with decreasing triangularity. This leads to a reduction of electron heat transport and therefore to an improvement in energy confinement for low collisionality plasmas.

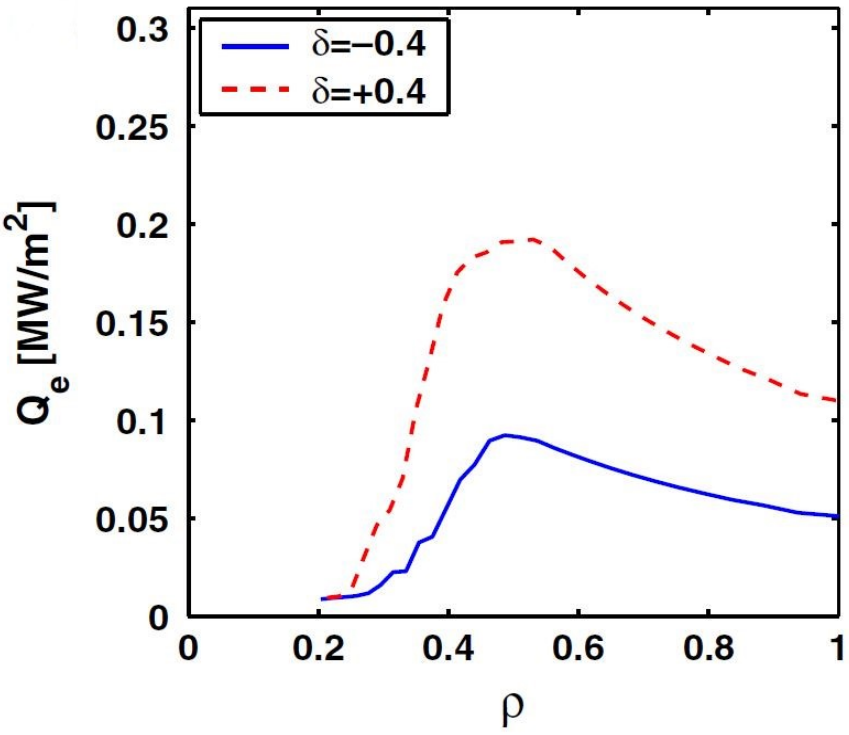

Figure 8: Electron heat flux for different triangularities (ρ being the normalized plasma radius) [20].

These results, as well as the conjectured dependence of sawtooth instability upon the geometrical factor [15], were numerically reproduced by means of gyrokinetic simulations [21] with a satisfactory quantitative agreement for non-linear simulations. Nonetheless, even if the beneficial effect of NTR was observed in ECH plasma, sawtooth were observed when the power deposition was moved towards the $q = 1$ rational surface and it was noticed that their crash amplitude was strongly triangularity-dependent for $\delta > 0.2$, while in the case of NTR it was smaller and decreased with increasing power.

Experiments were performed on DIII-D to validate and extend the results obtained on TCV [8]. Two heating phases were considered: pure ECH and ECH coupled with NBI. In both cases, reversing triangularity led to an increase of plasma stored energy. It was also observed that L- to H-mode transition power threshold was higher for NTR discharges. These discharges presented pedestal pressure profiles typical of L-mode, which did not trigger ELMs at all.

Figure 9 presents a comparison between experimental energy confinement time and ITER-89P scaling law. This figure could also be compared to figure 7 for TCV experimental results.

The deviation from the scaling law (red triangles in figure 9) of experimental results (blue ones) can be interpreted as a rough verification of the H-mode grade confinement. In fact the nearly constant slope indicates τ_E to be independent upon heating power. This feature is typically observed only in high

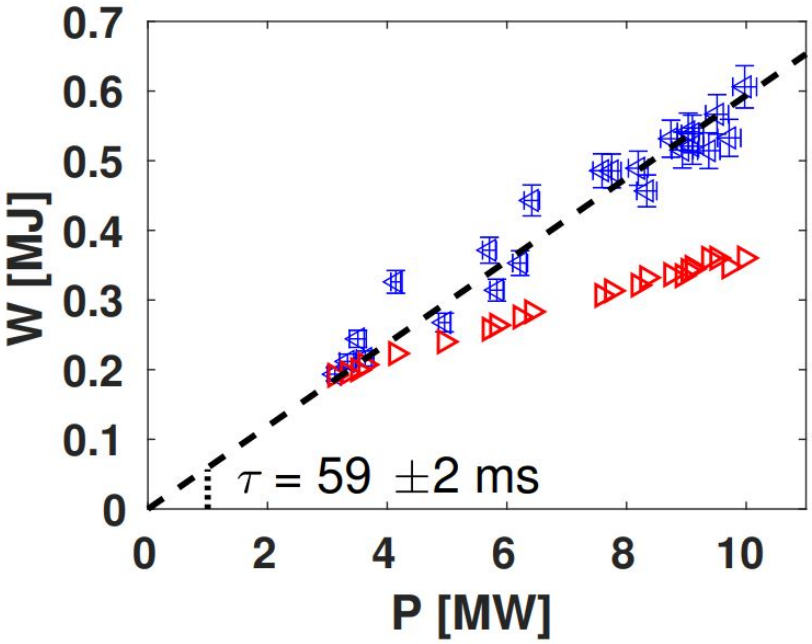

Figure 9: Fit to the ITER-89P (equation 44) mode scaling law of DIII-D experimental results. Blue triangles represents negative triangularity discharges of DIII-D, red squares the power scaling law ITER-89P. A least square fit (95% confidence) is provided. Errorbars come from a Monte Carlo analysis [8].

performance, H-mode plasmas [22].
Gyro-kinetic simulations showed that TEM are the dominant instability in these experiments too, for both the heating schemes. Also in this case, NTR plasmas presented weakened TEM growth rates, as a confirmation of results obtained by Marinoni [21] with $T_e > T_i$. These results for DIII-D, high beta plasma discharges confirmed what observed at TCV for the low beta cases.

3.2.2 *Effects of triangularity on ELMs mitigation and kink stabilization*

Concerning ELM mitigation, Pochelon et al. [16] investigated the ELM behavior for H-mode, highly collisional plasma discharges in negative triangularity configuration, in order to understand whether the advantageous effects of NTR for L-mode could be drawn out to H-mode. Results showed that NTR increased the frequency of type-I ELMs while their energy loss decreased. However, ELMs energy losses are reduced at the cost of a pedestal height reduction; therefore the core confinement is improved while edge confinement is weakened. Merle et al. [23] already demonstrated that tokamaks in negative triangularity configuration present a four times smaller pedestal height if compared to positive configurations in H-mode regime. Improved pedestal (and scrape-off layer) radiation for

sustaining a L-mode edge without ELMs is considered a key concept.
Minimization of ELMs energy bursts is required for ITER and their total elimination is necessary for DEMO and commercial-scale fusion reactors. For this reason, the power-handling assessment became the main way of thinking for reactor design. Kikuchi et al. [24] pointed out that TEM could be one of the most important instabilities for ECH plasmas leading to type-I ELMs.

Negative triangularity reactor

NTR plasmas present favorable features for ELMs behavior; moreover, negative triangularity tokamaks can be configured with optimized pressure gradient profiles, such as the one suggested by Kikuchi (figure 2a in [24]). This way, plasmas could be stable for $\beta_N > 3$ at moderate elongations, even in the absence of a magnetic well [25]. Nonetheless, low limit for β_N might pose a serious issue in NTR configuration, since it is given by the onset of unstable, low-n ideal XK due to the absence of a magnetic well for elongated cross sections.
Ren et al. [26] and Medvedev et al. [25] carried out numerical studies on two plasma discharges with different triangularities (one with strongly NTR, the other one with strongly PTR). The results showed that an ideal wall would only partly stabilize the XK for the NTR plasma, while its effect would be broader for a PTR one. This is due to the intrinsically different structure of the eigenmode: in the case of NTR, this instability is less "external" with respect to its positive counterpart, and the plasma displacement near the X-point(s) does not extend itself up to the plasma edge; this causes the NTR plasma to be less subject to wall stabilization. Moreover, the ideal wall beta limit is much larger for positive triangularity, and a closer wall would be required to achieve a similar value in NTR, posing the problem of heat flux impinging upon it [26]. It must be pointed out that toroidal flow might stabilize the XK, yet data showed its stabilizing effect to be similar for both configurations. In this study, kinetic effects were not taken into account, and their contributions could act on kink stabilization.
However, from an engineering point of view the space available near the X-point(s) for the NTR would lead to a more flexible divertor design, thus to a better heat exhaust handling, which is a crucial problem for conventional PTR configurations. Other means of XK stabilization can also be considered, such as the magnetic coils meant to be used for ELMs suppression. These coils might be used for feedback control, nonetheless they will probably be less accessible for reactor-scale devices. Therefore, "passive" XK control and stabilization are preferable [26].

3.2.3 *Reactor-relevant discharges in negative triangularity*

Recently, new experiments were carried out both on DIII-D [27] and on TCV [28].
The experiments on DIII-D were focused on exploring the feasibility of NTR L-mode discharges in SN diverted configurations. Among all the discharges, only one showed a transition to H-mode. Figure 10 features the total stored energy scaling law for NTR discharges of DIII-D. The agreement with previous experimental results, presented in figure 9, is clear to see.

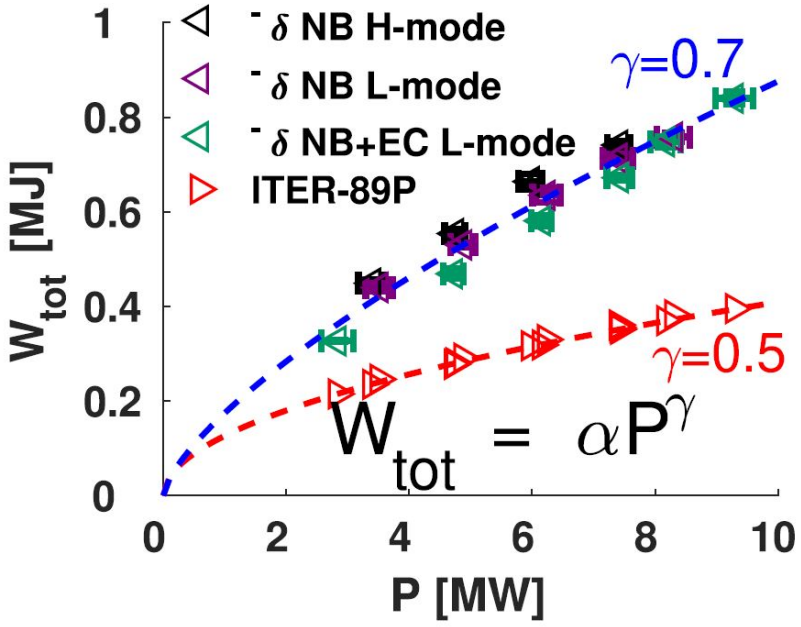

Figure 10: Total stored energy as a function of net auxiliary power for NTR discharges on DIII-D [27]. γ indicates a best fit estimate of the power degradation, corresponding to a power degradation of confinement equal to $\gamma - 1$.

The main difference is that in [8] the power degradation was almost zero (correlation was linear, hence $\gamma \simeq 1$). A possible explanation could be the greater value of δ in these experiments, which resulted in a confinement degradation. Another proposed explanation concerns the higher purity of plasmas in the experiments: impurities in plasmas have a stabilizing effect on ITG (ion temperature gradient) modes; moreover, the NBI heating was lower in this case, therefore modifying the electron-to-ion power ratio.
While it is clear that NTR stabilizes a TEM-dominated plasma [21], it is not yet clear to what extent NTR is capable to stabilize plasmas where ITG modes are dominant over TEM. Therefore, when the dominant ion-scale mode is ITG, as in the diverted discharges, the confinement scaling might as well differ from that in TEM dominated regimes. Furthermore, ELMs-free scenarios in future reactors should exhaust impurities and ashes in an efficient way. The impurity retention was less problematic in this case: particle-to-energy confinement time

ratio was measured to be of the order of unity for L-mode discharges, while in H-mode regimes this ratio typically ranges from 2 to 4.

TCV experimental campaign was devoted to characterize L-to-H transition power threshold as a function of plasma parameters.
Out of several hundreds of discharges with various power levels obtained with ECH coupled with NBI, only a few of them transitioned to H-mode.
A study of two symmetric diverted plasma discharges, one in NTR and one in PTR, was also carried out. The PTR discharge was representative of the ITER baseline scenario. This study has now confirmed that the energy confinement time remains better in fully NTR diverted configuration with respect to an equivalent PTR diverted plasma. The NTR case showed a smoother (though higher) pressure profile and sustained at twice the β_N for ITER with roughly one third the power supply, as presented in figure 11. However, it must be stated that in this work no diverted, high-β_N *stationary* plasmas have been obtained with auxiliary heating, being it NBI or ECH. Almost all the discharges presented a neoclassical $(m, n) = (2, 1)$ tearing mode disruptive instability.

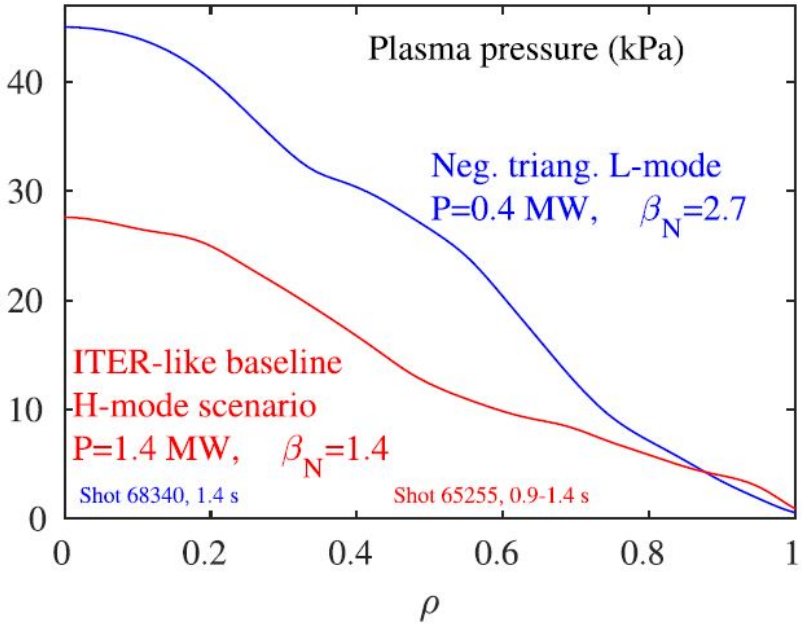

Figure 11: Pressure profile for ITER-like H-mode (red) and negative-triangularity L-mode (blue) (ρ being the normalized plasma radius) [28].

This work analyzes real plasma discharges in NTR configuration compared to their PTR counterparts. The next chapter features the numerical modeling and linear stability analysis of these discharges. The discharges come from experiments carried out on the TCV and RFX-mod machines in tokamak configuration; therefore, a brief description of the machines is hereunder provided.

3.3 TCV

TCV (fr.: Tokamak à configuration variable) is a Swiss research fusion reactor characterized primarily by extreme flexibility in plasma shaping and positioning. The main aim of TCV is to investigate effects of plasma shape on tokamak physics. This device has different heating systems: during most of the device's lifetime, its primary auxiliary heating source has been electron-cyclotron resonance heating (ECRH) with peak power up to $2.7MW$ for a $\sim 1m^3$ plasma; since 2015, neutral beam injection heating (NBI) has been employed too on TCV with a beam of maximum $\sim 1MW$ power [29] [30]. TCV is employed in many different research programs, from scenarios in support of ITER up to advanced tokamak scenarios. The experimental campaigns are assisted by a continuous program of diagnostic. A system of 16 independently-powered shaping poloidal-field coils provide the shaping versatility of the device.
The main operating parameters of TCV are resumed in table 1. It is clear that its strongest feature is the possibility to exploit a wide range of triangularities, in order to investigate stability of both positive and negative ones.

TCV device operating parameters	
Major radius R	0.88 [m]
Minor radius a	0.25 [m]
Max vacuum toroidal magnetic field B_ϕ	1.54 [T]
Max plasma current I_p	1.0 [MA]
Triangularity range δ	-0.7/+1.0
Elongation range κ	0.9/2.8
Max ohmic heating $P_{ohm,max}$	1.0 [MW]
Max NBI heating $P_{NBI,max}$	1.3(D)/1.15(H) [MW]
Average pulse duration τ	2 [s] (up to 4s)
Electron density n_e	$\sim 1 \cdot 10^{19}[m^{-3}]$
Electron temperature T_e	up to 15 [keV]
Ion temperature T_i	up to 2.5 [keV]

Table 1: TCV operating parameters provided by [29], [30] and [17].

3.4 RFX-MOD

RFX-mod (Reversed Field eXperiment) located in Padova (IT) was the biggest RFP (reversed field pinch) device active. The RFX-mod experiment was a device capable of operating both in RFP and in tokamak configurations. The main features of the device were plasma shape control, which was possible thanks to the PF coils power supply flexibility [31] [32], and the control capability of MHD instabilities thanks to the feedback system made of 192 independently driven active coils. It was operated to investigate a wide range of experimental conditions such as RFP, tokamak and the so-called "ultra-low-q" configurations. In RFP configuration, RFX-mod was devoted to enhance the understanding of the confinement properties at high current (up to $2MA$) [33]. Some enhancements for the RFX-mod device (which will become RFX-mod2 after upgrading) have been proposed and are, at present, in the final design phase.
The main operating parameters of RFX-mod are resumed in table 2.

RFX-mod device operating parameters	
Major radius R	2.0 [m]
Minor radius a	0.459 [m]
Plasma volume V_{plasma}	10 $[m^3]$
Max toroidal magnetic field B_ϕ	0.7 [T]
Max plasma current I_p	2.0 [MA]
Max pulse duration (RFP) τ_{RFP}	0.5 [s]
Max pulse duration (tokamak) $\tau_{tokamak}$	1 [s]
Max electron density n_e	$\sim 8 \cdot 10^{18} [m^{-3}]$
Max plasma temperature T_{plasma}	1.72 [keV]

Table 2: RFX-mod operating parameters provided by [31], [32] and [33].

4

NUMERICAL MODELING RESULTS

The equilibrium code CHEASE together with the linear-resistive stability code MARS-F have been used in order to carry out the stability analysis of plasma discharges. Both the codes are integrated in the OMFIT framework. A brief description of the codes can be found in Appendix A. The results of the numerical analyses are presented hereunder. The results of ideal stability are reported for each discharge, followed by the results of resistive stability.

4.1 TOWARDS HIGH PERFORMANCE NTR PLASMAS IN TCV

The first pair of plasma discharges analyzed is the #69273 at $t = 1.70s$ (NTR) - #69511 at $t = 1.50s$ (PTR). These discharges have been realized on the TCV machine keeping almost the same plasma current I_p and heating power P_h. The aim of having a couple of plasmas with similar parameters, yet different triangularity, is to investigate the influence of negative triangularity on stability and confinement compared to a positive counterpart.
Global MHD stability of these plasmas is investigated with parametric numerical studies, to confirm the experimental evidence suggesting that most of the disruptive shots terminate below the eventual β limit.
The parameters of these plasma discharges are listed in table 3, while their equilibrium configurations are presented in figures 12 and 13, respectively.

Discharge	#69273	#69511
Triangularity δ	-0.26	+0.35
Snapshot time instant t (s)	1.70	1.50
Type	Limiter	Limiter
Average electron density $< n_e >$ $(10^{19} m^{-3})$	4.6	3.4
Plasma current I_p (kA)	226	228
NBI heating power P_h (MW)	1.02	1.03
β_N	2.02	1.25
Elongation κ	1.26	1.34

Table 3: Plasma parameters of #69273-#69511 discharges (provided by [34]).

The value of q at the magnetic axis (q_0) is below unity for both the equilibria. This is consistent with experimental MHD spectra (from Mirnov coils) showing the so-called sawtooth activity, as shown in figures 14 and 15. From the point of

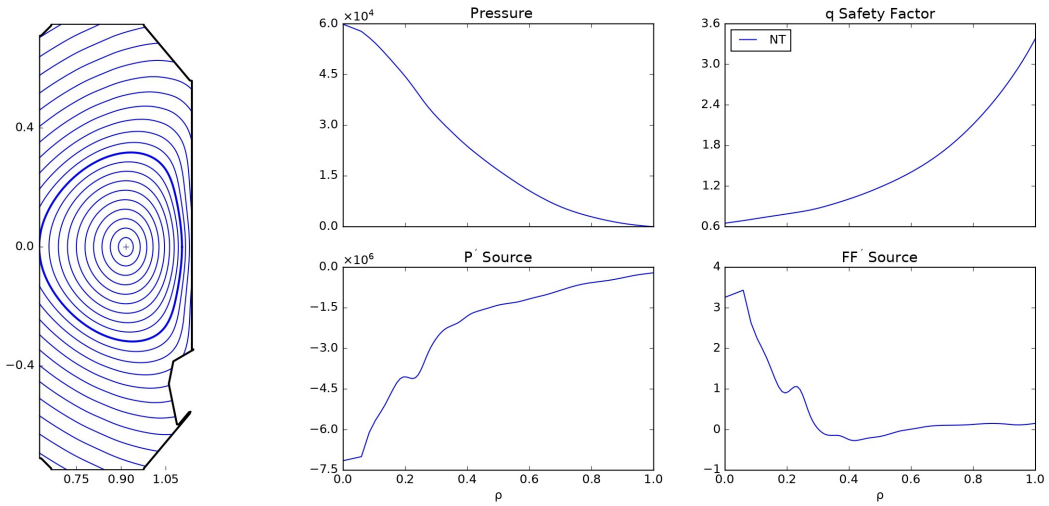

Figure 12: Equilibrium of #69273, negative triangularity discharge (EQDSK file).

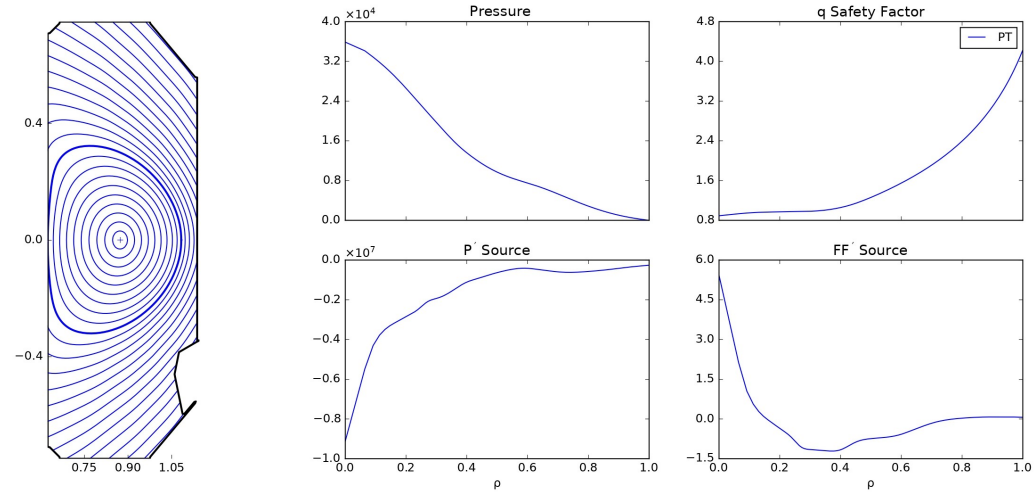

Figure 13: Equilibrium of #69511, positive triangularity discharge (EQDSK file).

view of ideal MHD, sawtoothing is reflected in the current-driven $(m, n) = (1, 1)$ internal kink. This has been removed with the procedure described below, in order to focus on $n = 1$, $m > 1$ modes. It is worth noting that this operation might affect important dynamics in the results, as will be briefly discussed later in the work.

In general, the PTR discharge presents a higher q profile with respect to the NTR case. In particular, the PTR case presents such a q profile that the rational value $q = 4$ is exceeded, while the NTR case reaches the value $q \approx 3.6$ as its maximum. This lower $q(a)$ value can contribute to a somewhat weaker global stability for the NTR equilibrium.

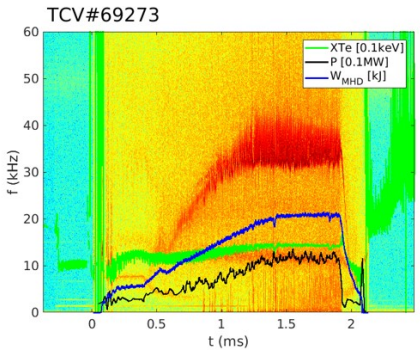

Figure 14: Spectrogram of odd-n modes for shot #69273.

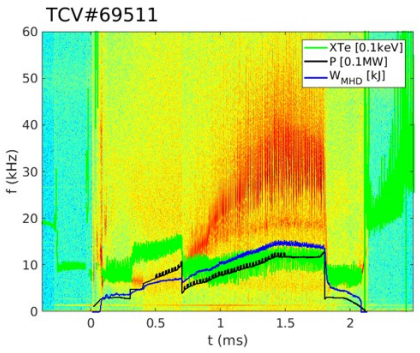

Figure 15: Spectrogram of odd-n modes for shot #69511.

4.1.1 *Ideal stability*

Figure 16 shows the profiles of safety factor q for both the discharges. In order to isolate possible tearing modes, safety factor profile q was numerically modified to make it larger than unity at every radius. In order to do this, the original current profile is interpolated with a target current profile numerically produced in such a way as to obtain a desired value of $q_0 > 1$. This modification is not uncommon: such an analysis with modified q profile was carried out by Marinoni et al. [8]. The modified q profiles are presented in figure 17.

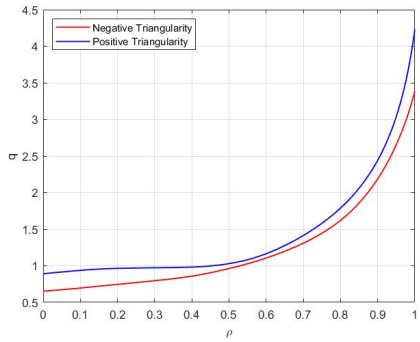

Figure 16: Safety factor q profiles of the #69273 - #69511 discharges.

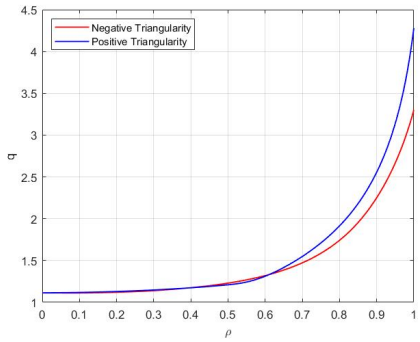

Figure 17: Modified safety factor q profiles for the #69273 - #69511 discharges.

The removal of the internal kink by raising q_0 above unity allowed to study the stability of pressure driven external kink modes. A scan in pressure is performed in order to determine the stability of the XK mode (referred to as no-wall limit). In a pressure scan, a set of equilibria is produced by exploiting the CHEASE feature of re-scaling the pressure and for each one the stability analysis is carried out, until the stability threshold is found. The growth rates obtained are plotted against the normalized beta. A workflow of this procedure can be found in Appendix B. The results obtained for the pressure scan can be appreciated in

figure 18, where the normalized growth rate of the $n = 1$ ideal kink is plotted against normalized beta. No significant differences emerge from this analysis: for both the discharges, the no-wall limit is around $\beta_N^{No-wall} \approx 2.3$; therefore triangularity does not influence the stability threshold of the ideal XK. For both these shots the experimental β_N values reported in table 3 are below the calculated stability limit. The edge value of q was held in high regard while performing pressure scans. Indeed, while increasing the equilibrium pressure, the other features are kept as constant as possible by imposing the total plasma current to be constant. This can be done within reasonable limits since the q profile will also change in the process. If, for example, q_{edge} varies and exceeds a rational value, an additional rational surface is "numerically brought" into the plasma, and this could enhance the equilibrium stability, voiding the analysis.

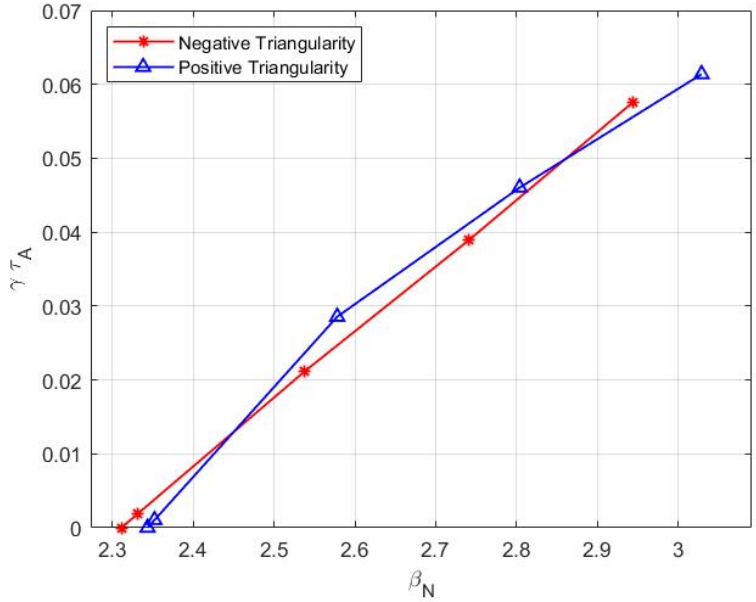

Figure 18: Growth rates of ideal (plasma resistivity $\eta = 0$) XK mode with varying plasma pressure of the #69273 - #69511 discharges.

4.1.2 *Resistive stability*

Resistive instabilities have been analyzed for #69273 - #69511 equilibria both with the original q profile and with its modified profile, in order to investigate and compare the stability of the TM. The Spitzer model has been implemented for plasma resistivity. A detailed description of the resistivity profile implementation in the MARS-F code is provided in Appendix C.

The analysis of TM is performed with the MARS-F code, where plasma resistivity is scanned, from high to small values. The growth rates obtained are plotted against the Lundquist number (on magnetic axis) $S = 1/\eta$, which is

used as a proxy to vary the whole resistivity profile. The results of the analysis for equilibria with $q_0 < 1$ are presented in figure 19. The growth rate remains almost constant for all the values of resistivity considered, thus suggesting that the instability found in the numerical analysis is not a TM, but rather an ideal mode (its growth rate is independent upon resistivity). In general, the growth rate of a TM should vary with varying resistivity (similarly to fig.1 in [35]). The nature of these modes can be understood by considering the eigenfunctions from MARS-F solutions, shown in figures 20, in terms of plasma displacement. These eigenfunctions are typical of internal kink instabilities (these do not cause the displacement of the plasma's outer surface, as the name suggests) since the dominant component is the $m = 1$ and it's located in the first rational surface. The three eigenfunctions considered are referred to the circled points in figure 19. In this case only the eigenfunctions for the NTR case are presented since the ones for PTR are essentially the same, thus suggesting that the triangularity does not influences these modes.

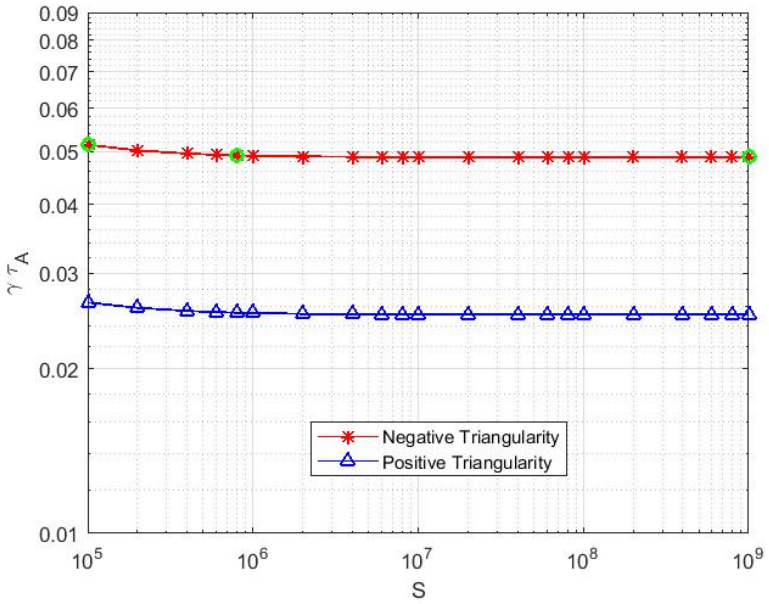

Figure 19: #69273 - #69511 growth rates scaling as function of the Lundquist number S for the original equilibria. The eigenfunctions related to the green dots are shown in figure 20.

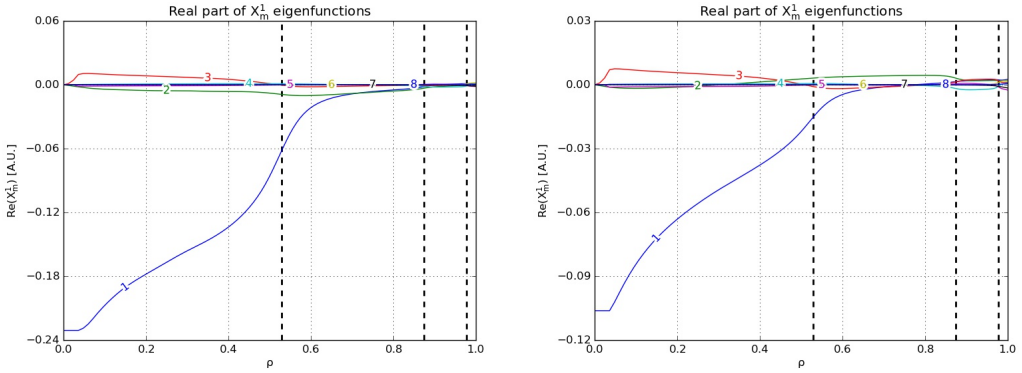

(a) (b)

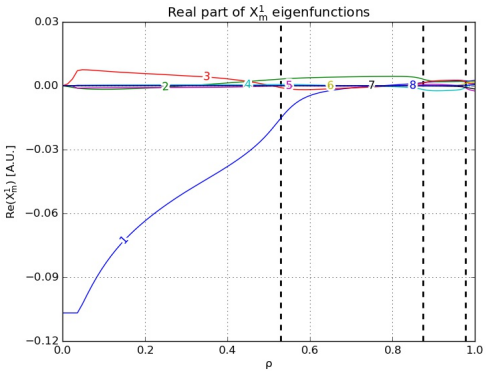

(c)

Figure 20: Plasma radial displacement eigenfunctions referred to the green dots in figure 19.

For the modified q equilibria, in the limit of $\beta \to 0$, both equilibria present an $n = 1$ unstable mode. In figure 21 the growth rate values obtained in the scan of TM for the NTR equilibrium are plotted against the S values. The classical scaling for the TM in the so-called "zero-β" limit is $\gamma\tau_A \sim \eta^{3/5}$ and it is here rather aptly recovered.

By looking at the spatial structure and poloidal components of the mode eigenfunction, it is clear that at very high resistivities ($S \sim 10^5 - 10^6$) the the behavior is dominated by the $m = 2$ harmonic located mainly at the first rational surface $q = 2$ (this can be found in figure 22); while at higher Lundquist numbers the main component becomes the $m = 4$ harmonic located at the second rational surface $q = 3$.

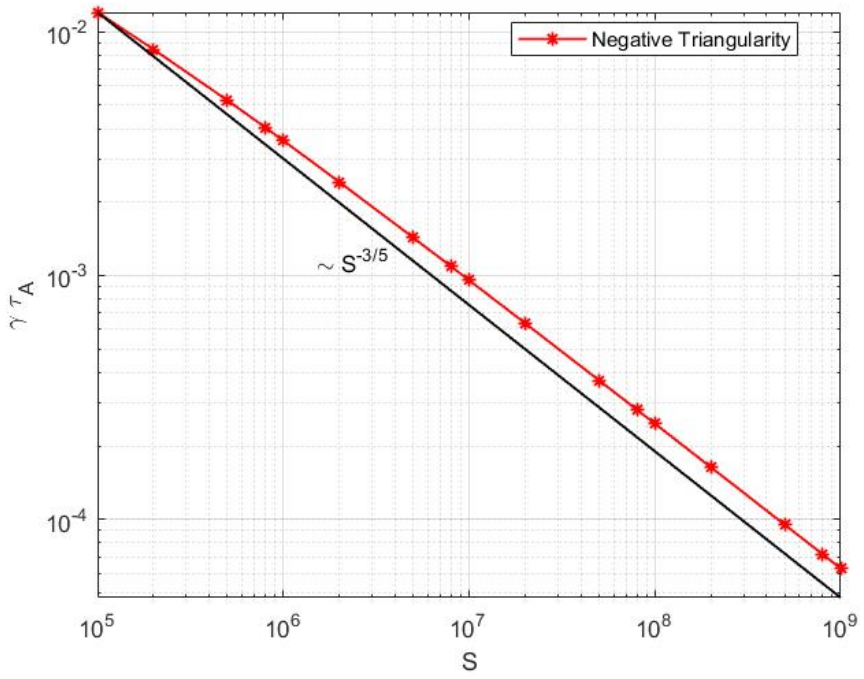

Figure 21: Growth rate of $n = 1$ tearing mode scaling with Lundquist number S of the #69273 (NTR) discharge for $\beta \to 0$ limit.

Almost the same considerations can be drawn for the PTR equilibrium (here the figure is not reported for the sake of conciseness), with the major difference that the growth rate is smaller with respect to the NTR case. This could be due to the fact that the PTR equilibrium presented an additional rational surface (the surface $q = 4$) which provided more stability to the mode; yet, none of them showed a completely stabilized behavior for the range of resistivity scanned. It should be noted that this analysis neglects the effects of pressure, which are usually stabilizing for the classical tearing mode [9]. This extra physical effect will be introduced in the following sections.

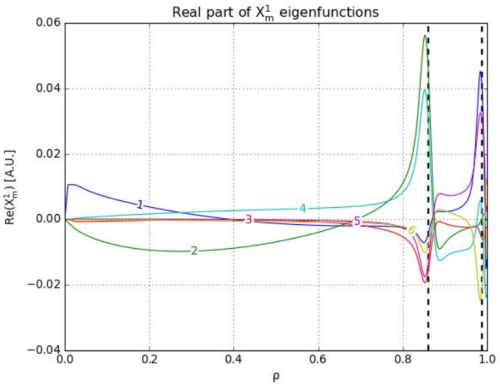

(a)

Figure 22: Radial displacement eigenfunctions for $\eta \sim 10^{-6}$. Only the first 6 harmonics are shown.

Figure 23 shows a comparison of the growth rates profiles. The experimental Lundquist numbers were almost the same for the two discharges, while the growth rate for the positive triangularity equilibrium present a lower value

with respect to its negative triangularity counterpart at each value of plasma resistivity considered in the scan.

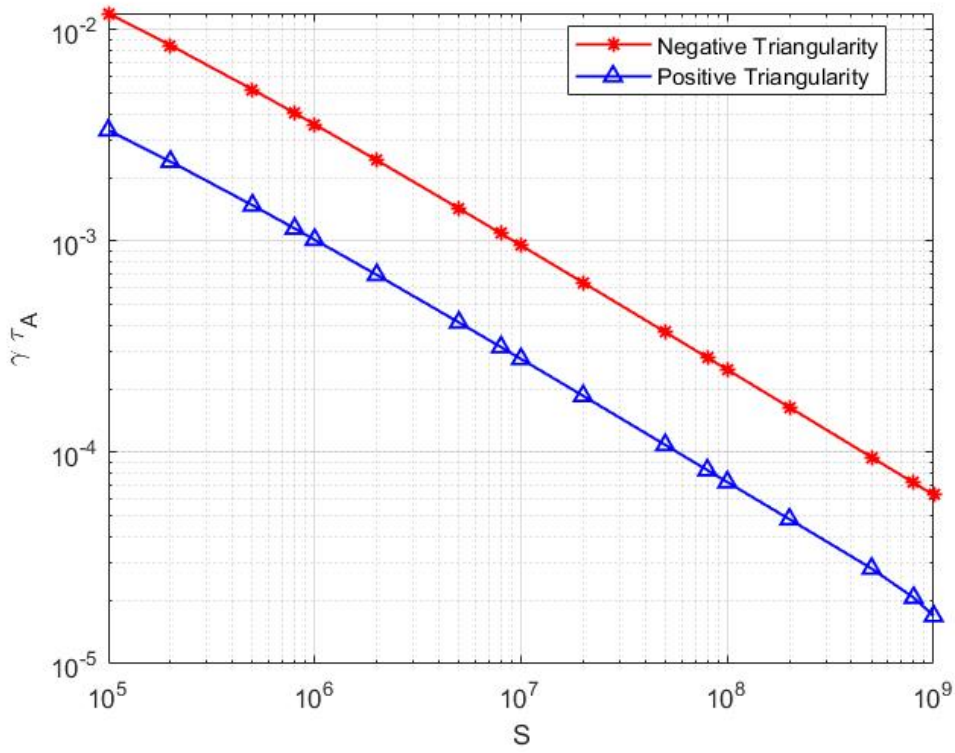

Figure 23: Comparison of growth rates of $n = 1$ TM for the #69273 - #69511 pair ($\beta \to 0$ limit).

When retaining equilibrium pressure, the linear resistive MHD simulations predict an unstable mode in the negative triangularity equilibrium, as presented in figure 24. This mode follows classical tearing mode scalings at lower resistivities, while at higher ones it follows the resistive internal kink scaling law $\gamma\tau_A \sim S^{-1/3}$ as described by Guo and Ma [36].
On the contrary, the mode is predicted to be stable at the experimental value of S for the PTR case, as shown in figure 25. Possible explanations can be found in physics that is not captured by the model, such as specific mode couplings or neoclassical effects (i.e. what is seen in experiments might be a NTM). Furthermore, equilibrium manipulations carried out to study these modes might themselves influence the results and explain deviations from experimental evidence in the PTR case.

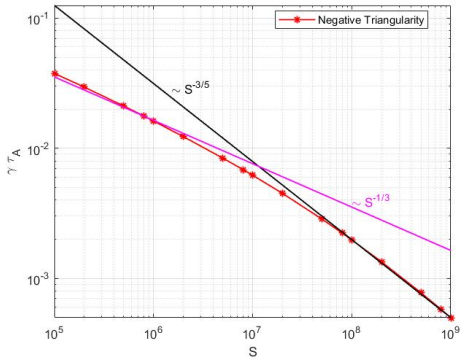

Figure 24: Growth rates of $n = 1$ tearing mode for #69273 discharge at experimental pressure. The two different scaling laws followed by this mode are reported.

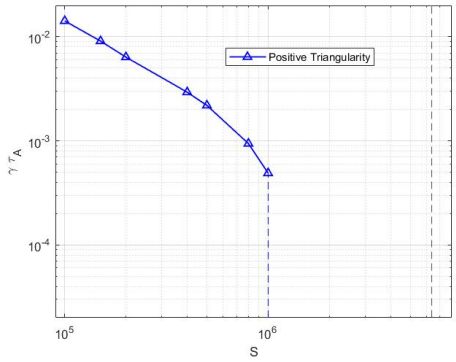

Figure 25: Growth rates of $n = 1$ tearing mode for #69511 discharge at experimental pressure. Dashed lines represent the experimental Lundquist number.

To conclude this section, the results obtained in the analysis of the two equilibria with $q > 1$ are summarized in table 4.

	#69273	#69511
Triangularity type	NTR	PTR
Experimental Lundquist number S	$6.6 \cdot 10^6$	$6.4 \cdot 10^6$
q_0	1.11	1.11
q_{edge}	3.30	4.28
$\beta_N^{No-wall}$	2.31	2.34
Zero-β TM stabilized	No	No
Exp. β TM stabilized	No	Yes [1], $\eta \sim 1 \cdot 10^{-6} \Omega m$

Table 4: Summary table for the results obtained for #69273 and #69511 equilibria. "Exp. β" stands for experimental β (therefore experimental pressure).

1 The mode is predicted to be stable by the numerical model, but experimentally the equilibrium is unstable. This could be due to neoclassical effects.

4.2 STABILITY OF SCENARIOS WITH ELEVATED q PROFILE

Recent experimental campaigns investigated the MHD phenomenology and dynamics in negative triangularity with elevated safety factor. The interest in these plasmas is connected to the development of hybrid scenarios and to the study of internal transport barriers.
What follows is the stability analysis of four of these recent discharges. Table 5 lists the plasma parameters.

Discharge	#73994	#73995	#73996	#73998
$< n_e > (10^{19} m^{-3})$	2	2	2.2	2.5-3
$I_p\ (kA)$	155	155	155	155
$P_{NBI}\ (MW)$	0	0	0.2	0.4
$P_{ECRH}\ (MW)$	2	2	2	2
β_N	0.69	0.97÷0.79 [2]	1.02	1.31

Table 5: Plasma parameters of #73994 - #73995 - #73996 - #73998 discharges (provided by [37]).

4.2.1 *Ideal stability: no-wall limit*

In the ideal MHD framework, discharges #73994, #73995 and #73996 were predicted to present almost the same stability thresholds for XK, being they similar in discharge parameters and safety factor profile, presented in figure 26. Due to the fact that all the plasma discharges presented a q_{edge} value very close to the rational value $q = 5$, while performing the pressure scan this value has been kept fixed in order not to create an additional rational surface. The analysis provides the stability thresholds for ideal XK within the range $2.2 < \beta_N^{No-wall} < 2.5$ (as shown in figure 27).

2 This equilibrium is considered at two different time instants, therefore two different values for the normalized beta are reported. The first refers to the snapshot at $t = 0.8s$, the second to the snapshot at $t = 1.3s$

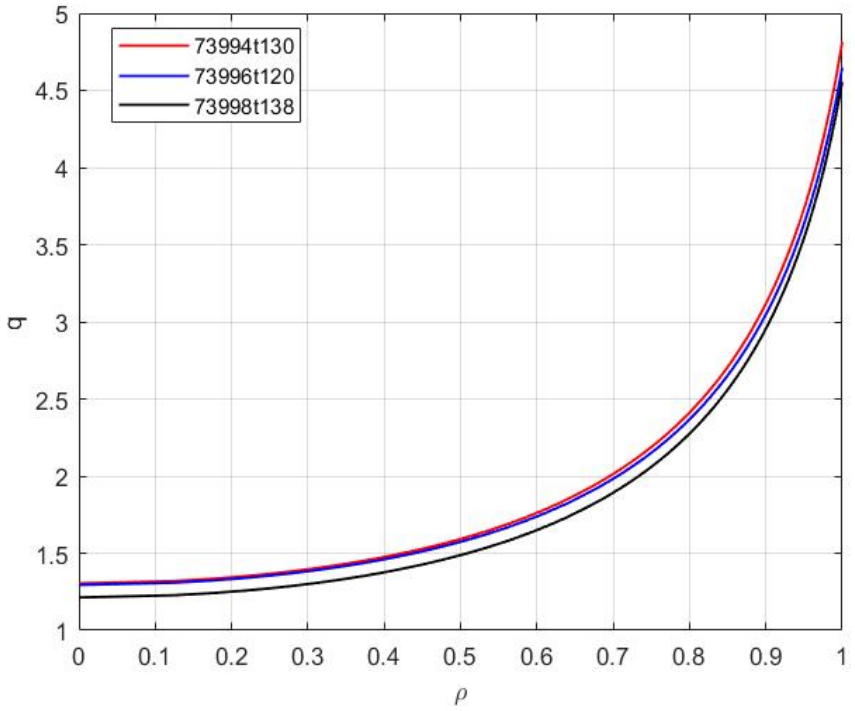

Figure 26: Safety factor q profiles of the #73994 - #73996 - #73998 plasma discharges.

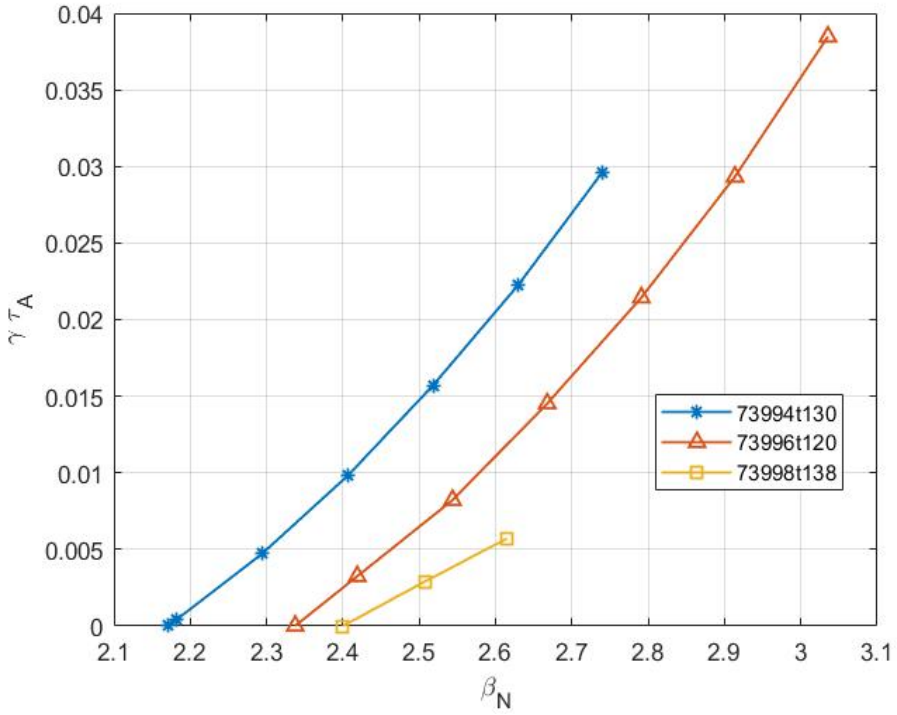

Figure 27: Growth rates of ideal XK mode with varying plasma pressure of the #73994 - #73996 - #73998 plasma discharges.

4.2.2 *Tearing mode analysis*

The analysis of the tearing mode considers the #73994 and #73995 discharges. In particular, in discharge #73995 the plasma vertical position was varied between $Z = 10cm$ and $Z = 0$. Two snapshots are modeled for this discharge, in order to investigate the effect of this sweep, considering the equilibria respectively at $t = 0.8s$ and $t = 1.3s$. #73994 is taken at $t = 1.3s$.
Figures 28 and 29 feature the q-profiles of the discharges. All the profiles present a q value at magnetic axis higher than unity and three rational surfaces ($q = 2, 3, 4$).

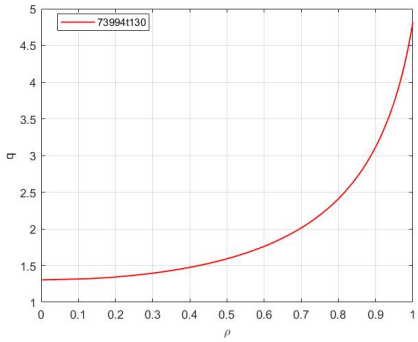

Figure 28: Safety factor q profiles of the #73994 plasma.

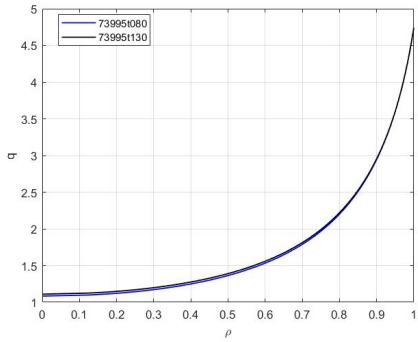

Figure 29: Safety factor q profiles of the #73995 plasma.

Figures 30 and 31 present the results of the analyses for the zero-β limit tearing mode. The Spitzer model has been utilized fors these analyses as well.
The scaling $S^{-3/5}$ is almost perfectly recovered, with a slight modification at high η values where the growth rates bend towards the resistive $(m, n) = (1, 1)$ IK scaling (this is reported as an example in the left-hand plot of figure 30); and with a perfect overlapping of the curves at lower resistivities. By looking at the components of the mode eigenfunctions, it is clear that at very high resistivities ($S \sim 10^5 - 10^6$) the behavior is dominated by a main $m = 2$ harmonic located at the $q = 2$ rational surface (this is legible from the rigth-hand plot of figure 30). This is in agreement with what would be expected for a $(m, n) = (2, 1)$ tearing mode. On the contrary, at lower resistivities the dominant harmonic turns out to be the $m = 4$. From a numerical point of view, the eigenfunction is in a "layer" around the rational surface (the resistive layer); in this layer the effect of resistivity is important, therefore it has to be properly solved by the usage of a fine space discretization in the radial direction. The mesh needs to be capable of resolving the layers at smallest resistivities too, which are the "narrower" ones.
In the considered range of resistivities, the TM is not stabilized.

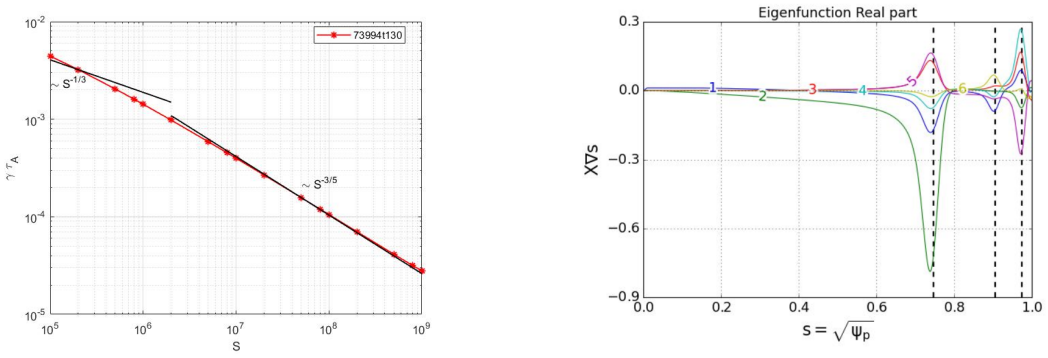

Figure 30: [Left] Growth rate of $n = 1$ tearing mode scaling with Lundquist number S of the #73994 at $t = 1.3s$ discharge ($\beta \to 0$ limit). [Right] First six harmonics of radial displacement eigenfunctions for $\eta = 5 \cdot 10^{-6}$. The dominance of the $m = 2$ harmonic can be clearly observed.

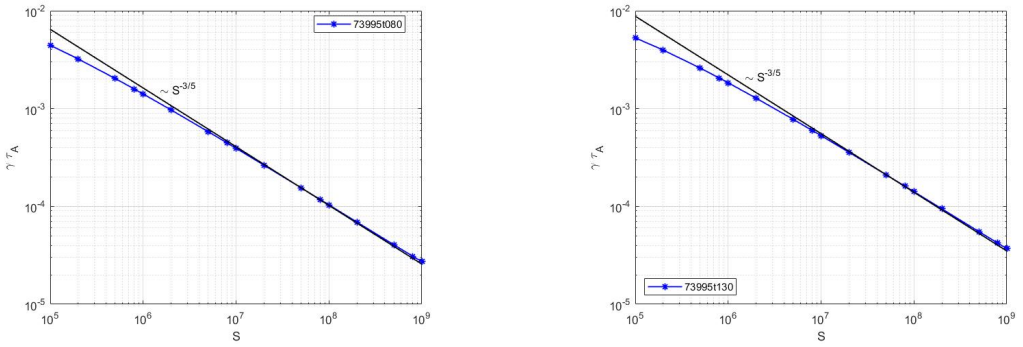

Figure 31: Growth rate of $n = 1$ tearing mode scaling with Lundquist number S of the #73995 discharges ($\beta \to 0$ limit). [Left] $t = 0.8s$. [Right] $t = 1.3s$.

The TM growth rates of the three equilibria presented above are collected in figure 32 with the aim of comparing them. $\gamma\tau_A$ for discharges #73994 and #73995 at first time snapshot are essentially the same; while moving from $t = 0.8s$ to $t = 1.3s$ the whole curve moves towards slightly higher growth rate values [38]. This could be due to the sweep of plasma vertical position performed during the discharge. However, the fact that the equilibrium is less stable at $t = 1.3s$ is confirmed by the analysis of the TM at experimental pressure presented below.

The stabilization effect at high Lundquist number is recovered when full equilibrium pressure is retained. This stabilizing contribution, often referred to as the Glasser-Greene-Johnson (GGJ) effect, is driven by pressure and toroidal curvature [9].

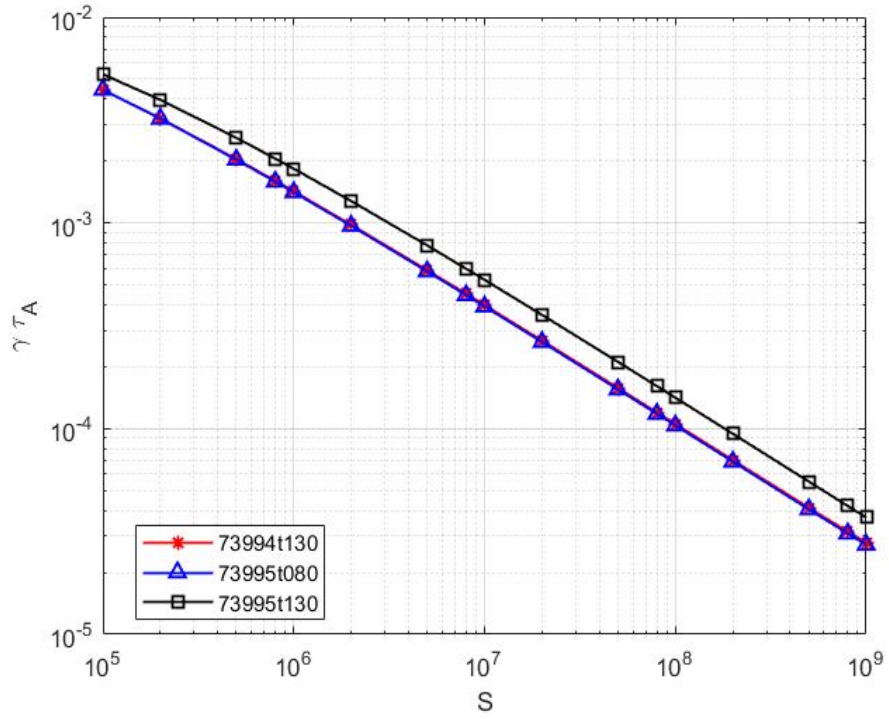

Figure 32: Comparison of growth rates of $n = 1$ tearing mode for #73994 and #73995 discharges at first snapshot for zero-β limit.

Stabilization of the mode occurs at $S > 1 \cdot 10^7$ for the first time snapshot and at $S > 2 \cdot 10^7$ for the second. This result is shown in figure 33: the TM of both the time snapshots for #73995 equilibria are collected together. It is interesting to notice the shift of the curve towards higher Lundquist numbers while moving from $t = 0.8s$ to $t = 1.3s$. This figure makes clear the loss of stability of the plasma at the second time instant. The reported behavior matches the experiment when looking at the first case, where the corresponding experimental Lundquist number is above the predicted stability threshold. The second snapshot, on the other hand, almost overlaps the experimental number: this result could be improved by tuning numerical resolution and/or using experimental data as input. Nevertheless the model successfully captures the behavior of the mode which is more unstable at $t = 1.3s$ with respect to the earlier time point.

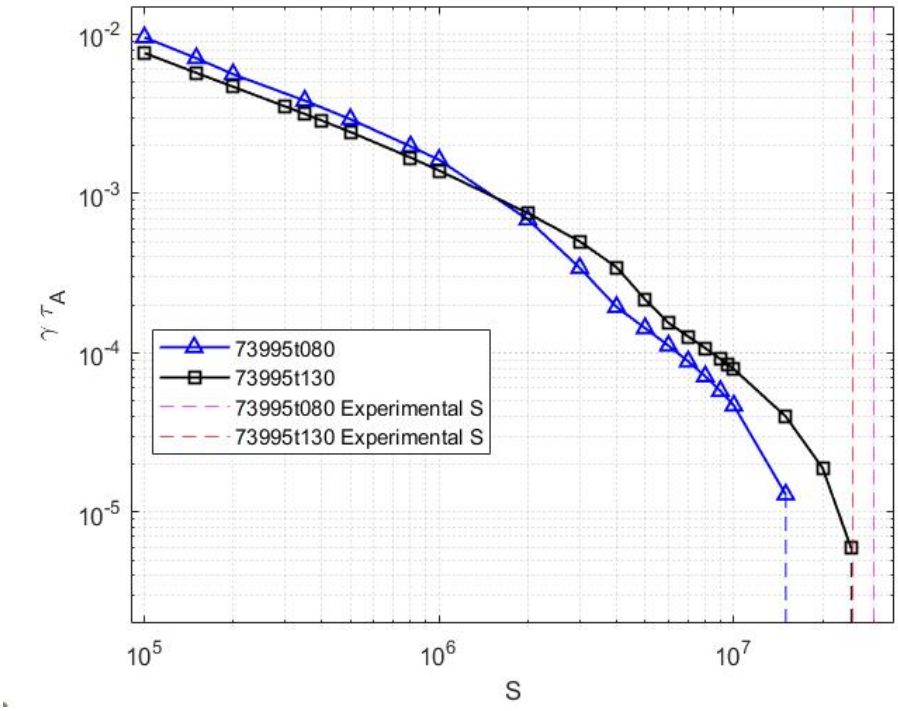

Figure 33: Comparison of growth rates of $n = 1$ tearing mode for #73995 discharge between $t = 0.8s$ and $t = 1.3s$, both including the effect of pressure. Dashed lines represent the experimental Lundquist numbers of the plasma discharges.

The fact that the curve "shifts" towards a more unstable mode is justified by the analysis of the spectrogram presented in figure 34. As reported, a mode with odd toroidal number is triggered during the sweep discussed above.

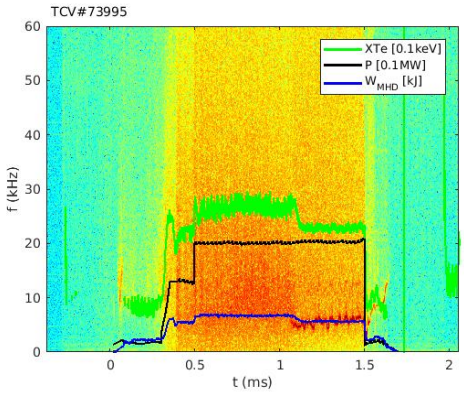

(a)

Figure 34: Spectrogram of odd-n modes for shot #73995 [38].

Finally it is also interesting to notice, in figure 35, the fact that for $S = 2 \cdot 10^7$ (which is a value above the Lundquist number value for the stability of #73995 at $t = 0.8s$) the growth rate decreases with increasing values of β_N, up to mode stabilization around the experimental normalized beta (blue curve). This trend has already been obtained in other numerical simulations as well, such as the ones carried out by Hao [39]. On the contrary, for lower values of S (i.e. higher resistivities) the mode undergoes an initial stabilization (red and green curve) with increasing pressure, while becoming more unstable while beta keeps on

raising. This could be due either to the transition to another mode or to a toroidal coupling with other harmonics coming into the eigenfunction while beta increases. It is worth noting that plasma shape (and therefore triangularity) has an effect on toroidal coupling.

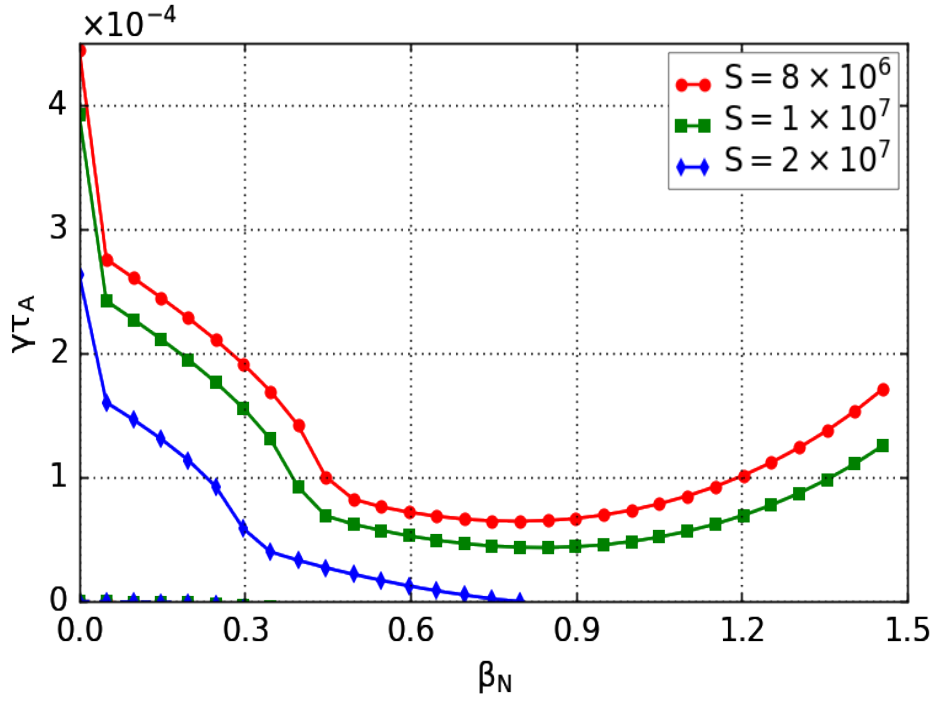

Figure 35: Growth rates of TM with varying plasma pressure of the #73995 at $t = 0.8s$ plasma discharge with different plasma resistivities.

4.3 COMPARISON BETWEEN H-MODE AND L-MODE PLASMAS

From discharge #39722 of RFX-mod the corresponding "mirrored" equilibria have been obtained by numerical modeling [40]. The discharge is taken at two different time instants: at the first snapshot the confinement is L-mode, while the second snapshot features an H-mode confinement. For all these four equilibria, a circular wall (representing the RFX-mod2 copper stabilizing shell) was added, in order to perform analyses imposing an "ideal wall" boundary condition (i.e. a very high value of the wall flux diffusion time scale τ_W was imposed). This was implemented to obtain results for the ideal case in view of future studies of the real plasma-wall distance effect on stability.

4.3.1 *H-mode plasmas*

The first pair of equilibria is shown in figures 36 and 37; these two presented high-q_0 and H-mode confinement.

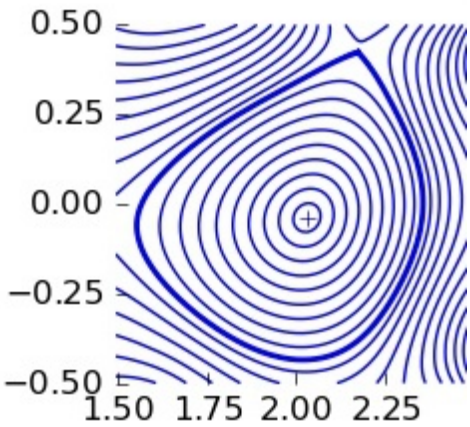

Figure 36: NTR H-mode 37992 RFX-mod equilibrium (EQDSK file).

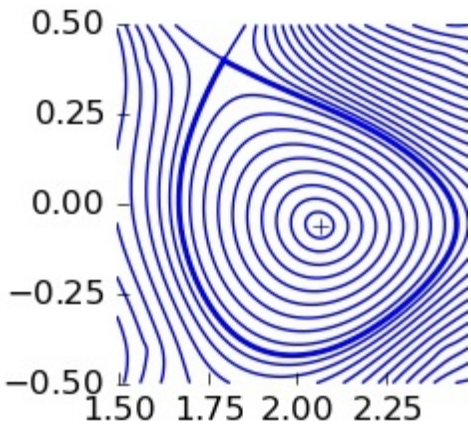

Figure 37: PTR H-mode 37992 RFX-mod equilibrium (EQDSK file).

A closer view of the q profile for those two equilibria is presented in figure 38. Both present a safety factor value at the magnetic axis greater than unity; therefore no ideal internal kink was expected to appear. A steep increase of the profile occurred near the q_{95} value ($q_{95} = q(\rho = 0.95)$). It is interesting to notice that, even if in general the q-profile for the negative triangularity equilibrium is higher, near the LCFS the positive triangularity q increases enough to outreach the negative one, presenting at last a higher value of the q_{edge}. Table 6 lists the most relevant values of the safety factor.
In the analysis of the resistive instabilities, the experimental profile of electron temperature was not available for these plasmas, therefore the Spitzer model was not implemented. In order to obtain useful results in view of RFX-mod2

	NTR	PTR
q_0	1.66	1.48
q_{95}	3.28	2.98
q_{edge}	4.47	4.99

Table 6: q values for RFX-mod H-mode equilibria.

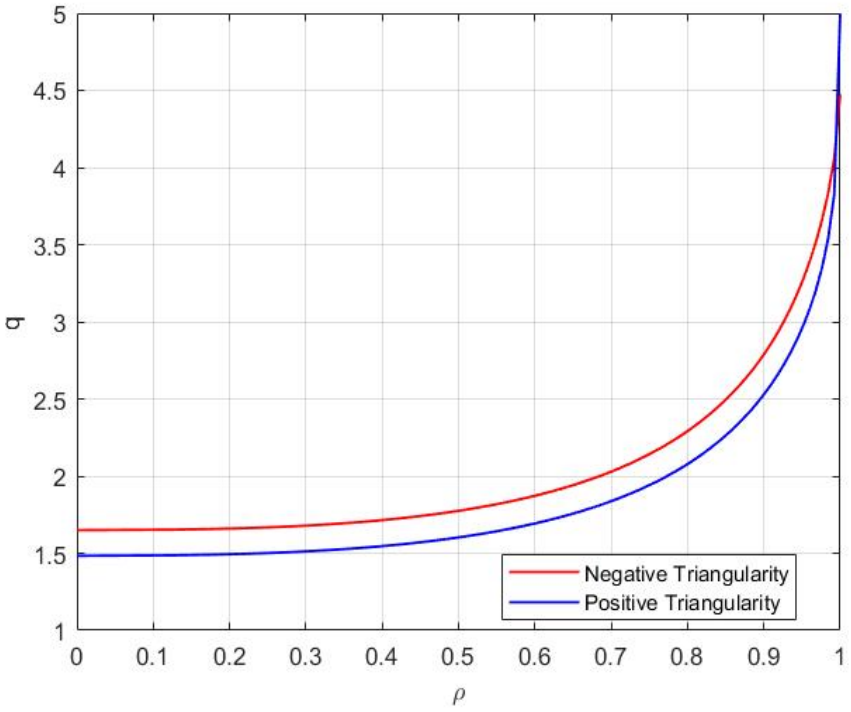

Figure 38: Safety factor q profiles of the RFX-mod H-mode plasmas.

plasmas, a resistivity constant along the plasma radius was utilized (see Appendix C and [41] for a more specific description).

In the limit of $\beta \to 0$, both equilibria present a $n = 1$ unstable TM mode which almost perfectly recovers the scaling $S^{-3/5}$, as shown in figure 39. In this case the equilibria show the same growth rates for this mode, therefore for the zero-β limit, the stability appears to be independent upon triangularity.
The NTR equilibrium presents an $m = 2$ dominant component of the mode at low Lundquist numbers, while the behavior of the mode is dominated by the $m = 4$ with a $m = 2$ harmonic on the rational surfaces $q = 2$ and $q = 4$ at higher Lundquist numbers ($S > 10^6$). Instead, the PTR case shows a mixing of $m = 2, 3, 4$ harmonics on the rational surfaces $q = 2$ and $q = 3$ for almost all the scanned points. In both these cases, the TM is not stabilized.

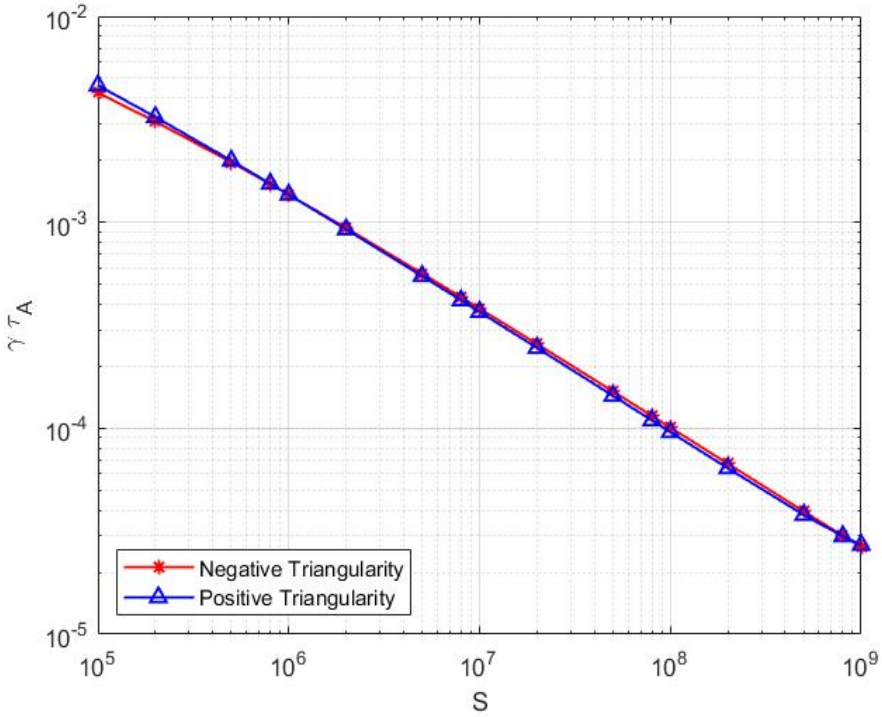

Figure 39: Comparison of growth rates of $n = 1$ TM for the RFX-mod H-mode plasmas ($\beta \to 0$ limit).

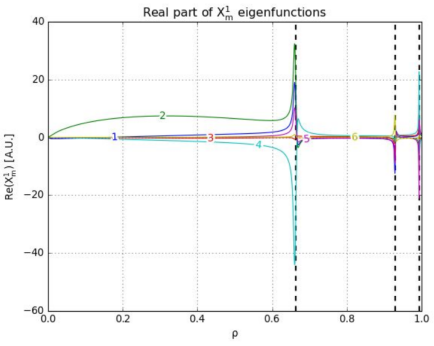

Figure 40: Eigenfunctions representative of the TM at $S = 5 \cdot 10^6$ for the NTR equilibrium ($\beta \to 0$ limit).

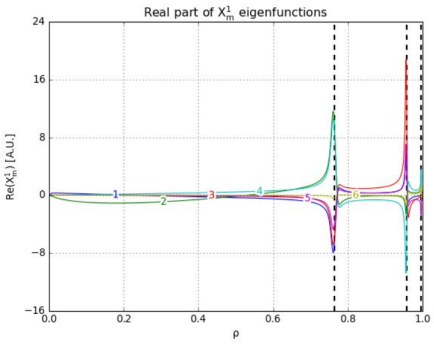

Figure 41: Eigenfunctions representative of the TM at $S = 5 \cdot 10^6$ for the PTR equilibrium ($\beta \to 0$ limit).

On the contrary, at the experimental pressure the growth rate of the most unstable TM for the NTR equilibrium is smaller than its positive counterpart and it stabilizes at higher values of resistivity, as clearly legible from figure 42. Also in this case, the GGJ effect can be considered the leading contribution to the stabilization of the mode.
Both the equilibria present a dominant $m = 2$ harmonic component around the $q = 2$ rational surface for all the scanned points. Since the rational surfaces are the same for them, plasma shape can be assumed to play a role in stabilizing the mode.

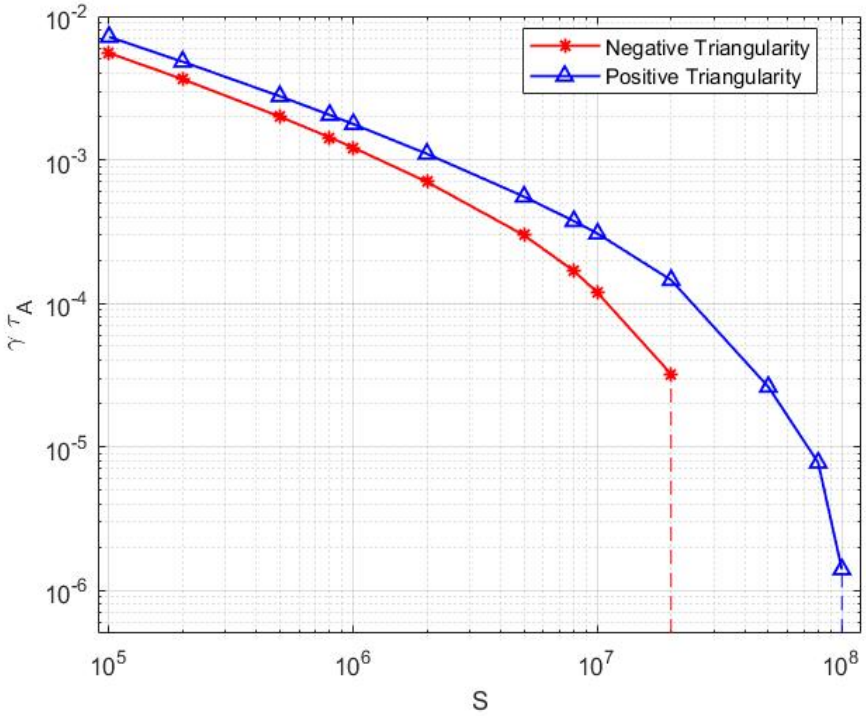

Figure 42: Comparison of growth rates of $n = 1$ TM for the RFX-mod H-mode plasmas at experimental pressure. Dashed lines represent a stabilization of the mode with null growth rate.

The effect of pressure can be appreciated in figures 43 and 44: at higher resistivities (corresponding to the first point of resistivity scan) the mode becomes unstable with increasing pressure for both triangularities, while at lower resistivities the stabilizing effect of pressure is clear, especially for the negative triangularity case. In particular, moving from the zero-β limit to small values of β (i.e. small values of the pressure), $\gamma\tau_A$ presents an initial steep decrease, then it keeps reducing with increasing pressure. This behavior has been already described and obtained in other numerical studies with similar modeling codes (see as an example figure 2 in [39]).

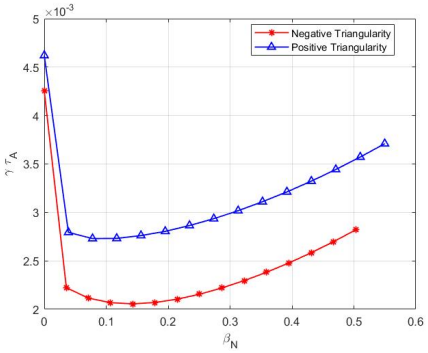

Figure 43: Growth rates of most unstable $n = 1$ resistive mode ($\eta = 10^{-5}\Omega m$) with varying plasma pressure, from zero to half the experimental pressure.

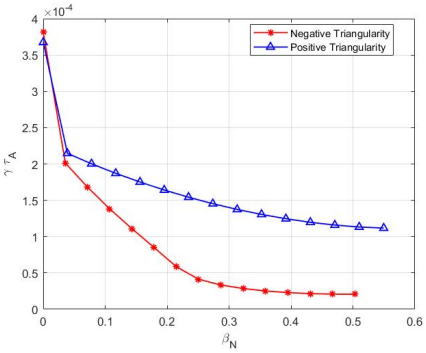

Figure 44: Growth rates of most unstable $n = 1$ resistive mode ($\eta = 2 \cdot 10^{-7}\Omega m$) with varying plasma pressure, from zero to half the experimental pressure.

Figures 45 and 46 depict the stabilizing effect of the pressure on the $n = 1$ tearing mode.

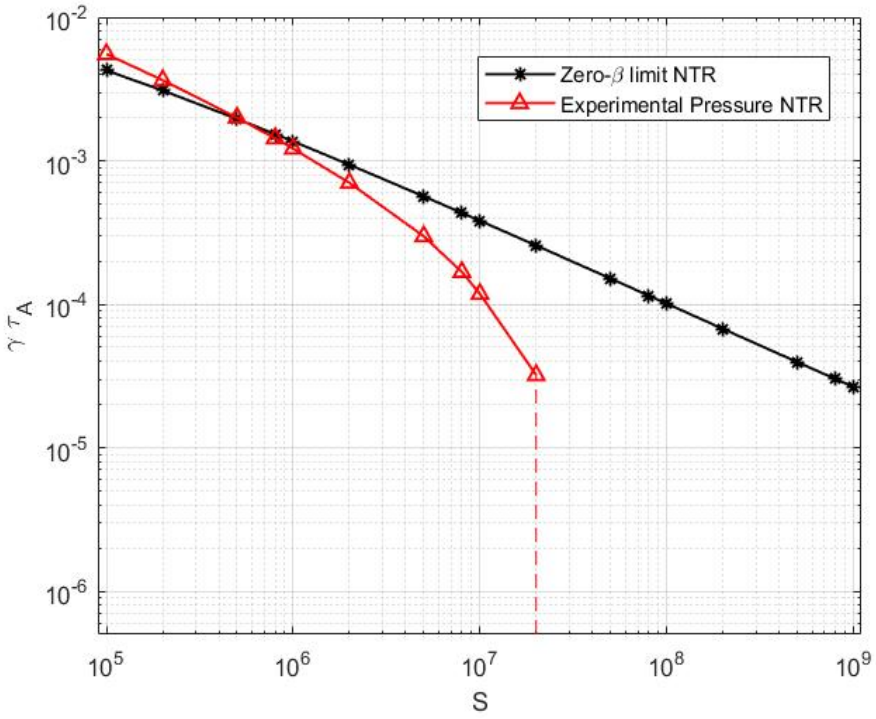

Figure 45: Comparison of growth rates of $n = 1$ TM for the RFX-mod H-mode NTR plasmas at $\beta \to 0$ limit and experimental pressure.

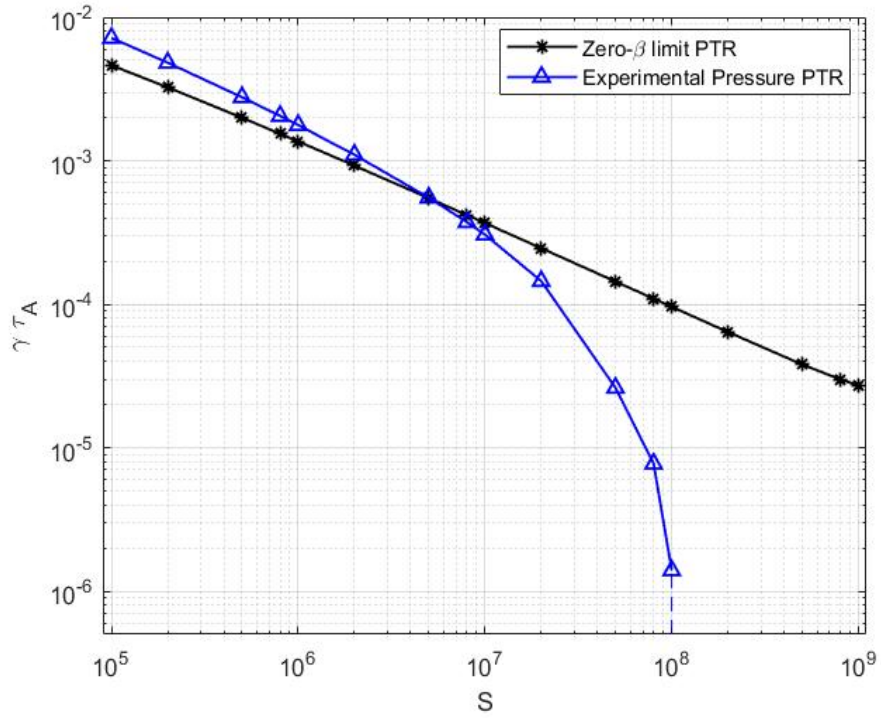

Figure 46: Comparison of growth rates of $n = 1$ TM for the RFX-mod H-mode PTR plasmas at $\beta \to 0$ limit and experimental pressure.

4.3.2 *L-mode plasmas*

The second couple of equilibria feature a $q_0 < 1$ and L-mode grade confinement; the equilibria are shown in figures 47 and 48.

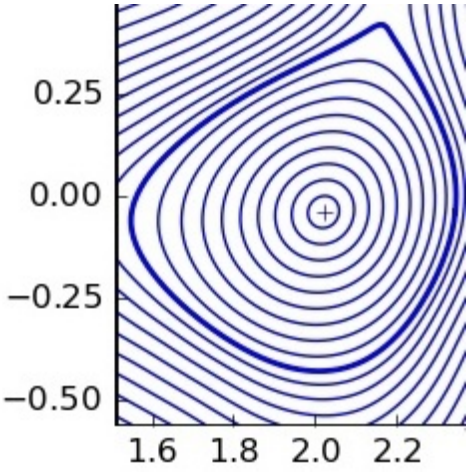

Figure 47: NTR L-mode 37992 RFX-mod equilibrium (EQDSK file).

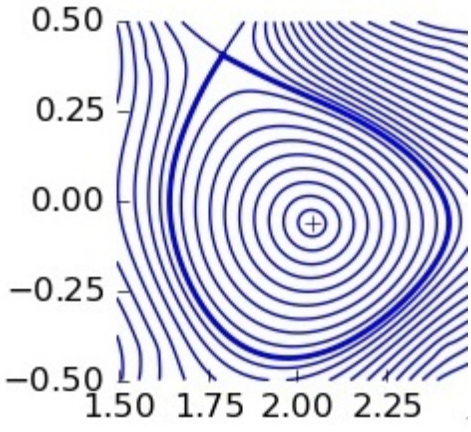

Figure 48: PTR L-mode 37992 RFX-mod equilibrium (EQDSK file).

Figure 49 presents the q profile for these two equilibria. This case as well shows that the positive triangularity q-profile increases near the LCFS enough to outreach its negative counterpart. Table 7 lists the most relevant values of the safety factor.

	NTR	PTR
q_0	0.70	0.68
q_{95}	3.10	3.01
q_{edge}	4.85	5.25

Table 7: q values for RFX-mod L-mode equilibria.

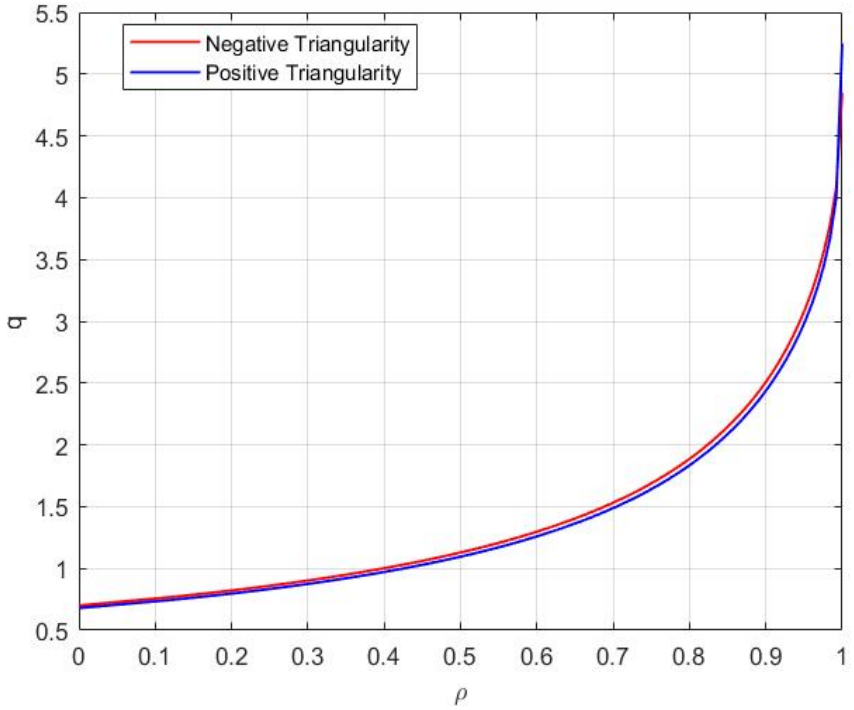

Figure 49: Safety factor q profiles of the RFX-mod L-mode plasmas.

Since in these equilibria the safety factors assume values smaller than one at the magnetic axis, the presence of an ideal IK was expected for both. Its stability with varying pressure is analyzed in a pressure scan imposing no resistivity to the plasma and disregarding the presence of the wall; the results are presented in figure 50. The growth rate of this mode is almost similar and it gets stable at $\beta \simeq 0.3$.

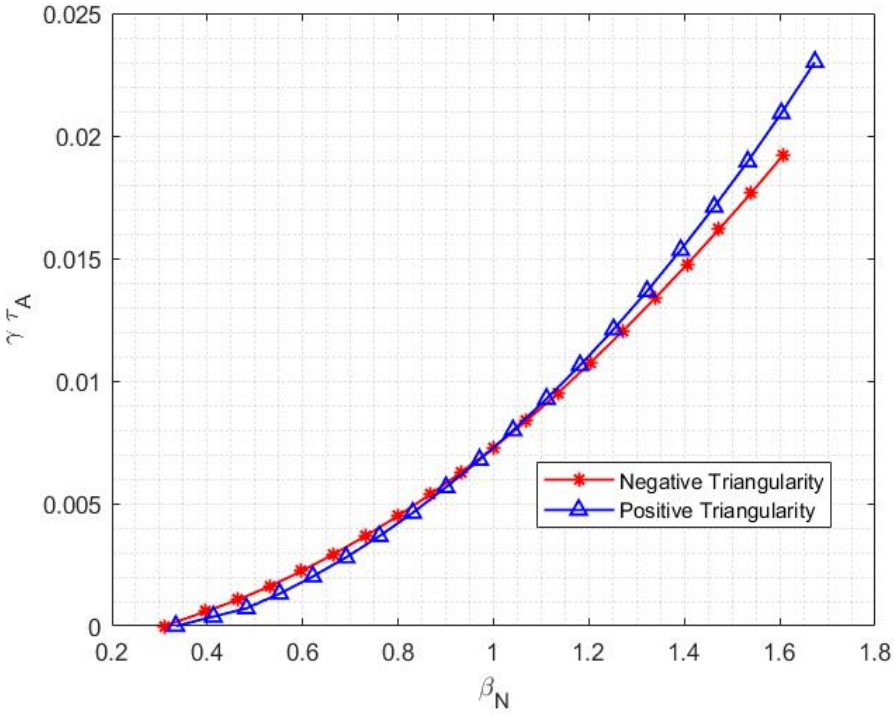

Figure 50: Growth rates of ideal IK mode with varying plasma pressure for the L-mode RFX-mod plasmas.

In the limit of $\beta \to 0$, the $n = 1$ unstable TM mode is shown in figure 51. This figure shows that both the equilibria present almost the same growth rate for this mode, hence the stability appears to be again independent upon triangularity. Nonetheless, it is noticeable that the L-mode plasmas present a growth rate for this mode smaller than their H-mode counterparts (figure 39 seen above).

The main difference with respect to the H-mode equilibria is that the curves "bend" at lower resistivities. This behavior could be due to the numerical modeling and it is still under investigation. Both the TM behaviors are dominated by the $m = 4$ component located at rational surfaces $q = 2$ and $q = 3$ at all the points; hence this bending effect can be considered to be independent upon triangularity and eigenstate. This effect has already been seen in other stability analyses and it is still under investigation.

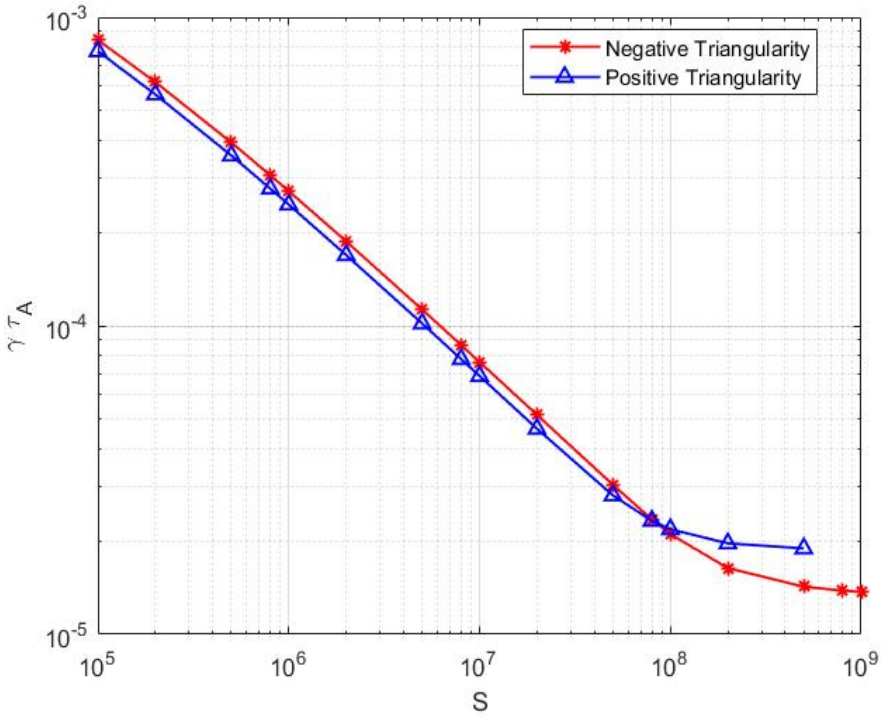

Figure 51: Comparison of growth rates of $n = 1$ TM for the RFX-mod L-mode plasmas ($\beta \to 0$ limit).

To conclude this section, the results obtained for the two pairs of equilibria are summarized in table 8. The choice of not performing the analysis for the TM in L-mode plasmas was driven by the lack of experimental results as a validation of the analysis.

	H-mode		L-mode	
Triangularity type	NTR	PTR	NTR	PTR
δ	-0.35	0.43	-0.35	0.38
β_P	0.89	0.92	0.71	0.72
$I_p(kA)$	62.42	62.42	61.05	61.05
Zero-β TM stabilized	No	No	No	No
Exp. β TM stabilized	Yes, $\eta \sim 5 \cdot 10^{-8} \Omega m$	Yes, $\eta \sim 1 \cdot 10^{-8} \Omega m$	*	*
IK stabilizing β_N	not present	not present	~ 0.3	~ 0.3

Table 8: Summary table for the results obtained for 39722 and mirrored equilibria (plasma parameters are provided by [32]). "Exp. β" stands for experimental β while stars distinguishes a not performed analysis.

5

DISCUSSION AND OUTLOOK

The equilibrium code CHEASE and the linear stability code MARS-F have been used to carry out the analysis of recent TCV experiments and the modeling of RFX-mod plasmas, with a projection to RFX-mod2. The goal was to assess whether or not the plasma shape, in particular triangularity, could affect the behavior of instabilities.
The results show that triangularity does not significantly affect the structure and dynamics of ideal modes. Also the stability threshold of pressure-driven external kinks are found to be similar when modeling comparable equilibria with positive or negative triangularity. On the contrary, triangularity can indeed play a role in stabilizing resistive modes with toroidal mode number $n = 1$, often identified as tearing modes.

For the high β TCV equilibria, a dedicated modeling strategy has been adopted to isolate the physics of external kink modes first and tearing modes afterwards. In particular the $q = 1$ surface has been removed from the considered equilibria in order to focus on other instabilities. The investiagated equilibria present almost the same plasma current and heating power. The positive triangularity equilibrium turns out to be more stable against tearing modes, and this could be due to the additional rational surface it exhibits. Both the equilibria present almost the same β value for XK stabilization. The numerical model recovered the expected behavior of classical tearing modes for the zero-β limit as function of resistivity.
The high q equilibria do not have a positive counterpart to be compared with. These have been extracted from very recent experiments, carried out during the TCV campaign in Spring 2022, and this thesis work is the first systematic stability study of the results. The equilibria present values for the no-wall β limit in the range $2.2 < \beta_N^{No-wall} < 2.5$. Besides, a resistive kink behavior is found in some of the analyses, in particular towards very high (i.e. $\sim 10^5$) Lundquist numbers; this kink presents a different scaling law for the growth rate as a function of the resistivity. In this case too, the model aptly recovered the behavior of tearing modes in the zero-β limit case, especially at lower resistivities. Furthermore, MARS-F calculation (when the pressure contribution is included in the TM analysis) is in good agreement both with the well-known Glasser-Greene-Johnson [9] stabilizing effect and with evidence of destabilization of the tearing mode from the first to second time instant considered, as discussed in [38]. Finally, the analysis of the growth rate of TM with varying pressure instead of resistivity shows an initial stabilization of the mode which degrades when pressure keeps increasing; this could be due either to the transition to

another mode or to toroidal coupling (and in this case it would be affected by triangularity). Still, the behavior predicted by Hao [39] is once again found.
RFX-mod tokamak plasmas, and possible projections to RFX-mod2, are studied with two couples of equilibria. The first couple consists of a NTR and a PTR plasmas with H-mode confinement, while in the second the plasmas are in L-mode confinement. H-mode equilibria do not present ideal nor resistive internal kinks. The tearing mode analysis results show that for zero-β limit the growth rates are almost the same, showing an independence upon triangularity; on the contrary the negative triangularity equilibrium is more stable when pressure is re-introduced in the analysis. Both the H-mode equilibria stabilize at experimental pressure. The L-mode equilibria feature an ideal internal kink due to the safety factor value below unity at magnetic axis; yet the IK stabilizes at $\beta \simeq 0.3$ for both triangularities. Tearing mode analysis shows again an independence upon triangularity.

To conclude, the results achieved in this work indicate that triangularity plays a role in the stability of resistive modes, and possible beneficial effects of negative triangularity. An interesting quantitative result has been obtained by modeling the destabilization of $n = 1$ tearing mode in recent TCV experiments. On the other hand, no significant effect has been found for ideal modes, which is consistent with similar recent results with comparable physical models. Also, the analyses show that negative triangularity plasmas can achieve acceptable β values for the XK no-wall limit. A possible interpretation of the obtained results is that negative triangularity does not appear to negatively affect global plasma stability, at least using the physical models presented in this work. Investigation of possible effects would therefore require to go beyond ideal and resistive MHD, including for example drift-kinetic contributions.
A comparison with positive triangularity plasmas with elevated q profile will be useful to assess the effect of δ on modes that are located on outer rational surfaces. Also the analysis of L-mode plasmas with different triangularities (ranging from positive to negative values) exploiting the flexibility of TCV might be of use to comprehend how the triangularity influences the modes located inside the inner rational surface.

APPENDIX A

CHEASE

The CHEASE code (Cubic Hermite Element Axisymmetric Static Equilibrium, [42]) solves the Grad-Shafranov equation for toroidal MHD equilibria with pressure, current profiles and plasma boundaries specified by analytical forms or sets of experimental data points. CHEASE is a fixed-boundary code: the plasma boundary is specified by the last closed flux surface.
The Grad-Shafranov equation is solved in variational form. The discretization uses a bicubic Hermite finite elements with continuous first order derivatives for the poloidal flux ψ.
The nonlinearity of the problem is handled by Picard iterations. The mapping to flux coordinates is carried out with a method which conserves the accuracy of the cubic finite elements.

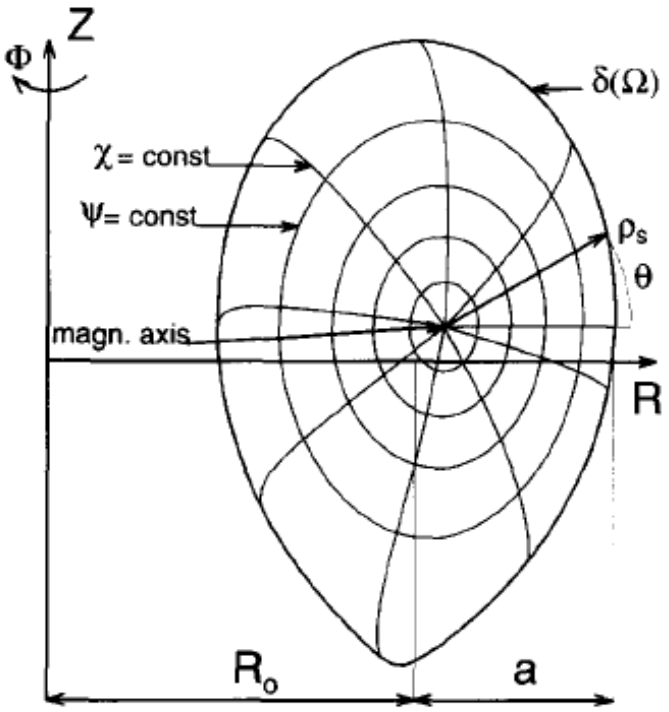

Figure 52: Flux coordinates in toroidal geometry [42].

In figure 5 the flux coordinates $(s(\psi), \chi, \phi)$ used in CHEASE are presented. Namely:

- the $s(\psi)$ coordinate is defined as

$$s = s(\psi) = \sqrt{\frac{\psi_{edge} - \psi}{\psi_{edge} - \psi_0}} \tag{47}$$

  where ψ_{edge} is the flux at plasma boundary, and ψ_0 is the flux at the magnetic axis. In CHEASE, equilibrium profiles are given as functions of s;

- χ is a generalized poloidal angle. It accounts for the boundary curvature, in order to have a uniform mesh. It is demanded to increase by 2π per poloidal turn;

- ϕ is the toroidal angle.

There are many different ways of defining the two free functions $p'(\psi)$ and $f(\psi)f'(\psi)$, defined in chapter 2. CHEASE can treat three different options for specifying the current profile. Profiles can be prescribed for each of the following:

1. $ff'(\psi)$
2. the surface averaged current density $I^*(s)$
3. the surface averaged parallel current density $I_{//}(s)$

If either one among 2) or 3) is specified, it is possible to evaluate the toroidal current density $\jmath_\phi$ and solve the Grad-Shafranov equation by two nested Picard iterations. For the sake of simplicity, all the passages are not reported here (see [42]).
The variational form of the Grad-Shafranov equation solved in CHEASE is:

$$\int_\Omega \frac{1}{R}\vec{\nabla}\varphi \cdot \vec{\nabla}\psi dS + \int_\Omega \varphi \jmath_\phi dS = 0 \tag{48}$$

where φ is an arbitrary weighting function from the same vector space of ψ. Equation 48 is solved numerically in the standard manner of the finite element method, by expanding ψ in Hermite bicubics on the rectangular grid (σ, θ), related to the cylindrical coordinates (R,Z) by:

$$\begin{aligned} R &= R_c + \sigma\rho_s(\theta)cos(\theta) \\ Z &= Z_c + \sigma\rho_s(\theta)sin(\theta) \end{aligned} \tag{49}$$

with

$$\begin{aligned} 0 \leq \sigma \leq 1 \\ 0 \leq \theta \leq 2\pi \end{aligned} \tag{50}$$

σ is a sort of normalized radius, while (R_c, Z_c) is the origin of the polar coordinates.
The unknowns of the discretized equilibrium problem are the values of the function ψ, its first derivatives with respect to σ and θ and the mixed second derivative. The integrals are evaluated numerically using Gaussian quadrature. In the Picard iterations, the (k+1)-th iteration is computed from the solution of the k-th iteration:

$$\int_\Omega \frac{1}{R}\vec{\nabla}\varphi \cdot \vec{\nabla}\psi_{k+1} dS = -\int_\Omega \varphi \jmath_\phi(\psi_k) dS \tag{51}$$

The Picard iteration is interrupted when:

$$\|\psi_{k+1} - \psi_k\| < \varepsilon \tag{52}$$

where ε is a predefined tolerance.

MARS-Q

MARS-Q is a modular, linear MHD stability code [43] which can also simulate plasma response to external fields, drift-kinetic effects on mode stability and quasi-linear evolution of plasma rotation. This work makes use of the "fluid" resistive MHD stability core module. This is commonly known as MARS-F. The MARS-F code calculates eigenmodes in 2D axisymmetric toroidal equilibria; it is capable of modeling MHD instabilities with low, intermediate and high toroidal mode numbers. The code solves the following equations for the perturbed quantities (indicated with the "1" subscript) over an $n = 0$ equilibrium (perturbations are assumed with single n toroidal periodicity):

$$\begin{aligned}
\gamma\rho_0\vec{v}_1 &= \vec{j}_1 \times \vec{B}_0 + \vec{j}_0 \times \vec{B}_1 - \vec{\nabla}p_1 \\
\gamma\vec{B}_1 &= \vec{\nabla} \times (\vec{v}_1 \times \vec{B}_0) - \frac{1}{\mu_0}\vec{\nabla} \times (\eta\vec{j}_1) \\
\mu_0\vec{j}_1 &= \vec{\nabla} \times \vec{B}_1 \\
\gamma p_1 &= -\Gamma p_0 \vec{\nabla} \cdot \vec{v}_1 - \vec{v}_1 \cdot \vec{\nabla}p_0
\end{aligned} \tag{53}$$

It is interesting to notice that MARS-F can handle a non-ideal plasma too, since the $\eta\vec{j}$ term appears in the system of equations.
MARS-F uses the same flux coordinates $(s(\psi), \chi, \phi)$ introduced above. Furthermore, it follows an iterative scheme too, in order to converge to a given eigenvalue, starting from an initial guess.
The MARS-F code is designed to work with a FE discretization in the radial direction, and a spectral discretization in the poloidal one.

OMFIT

The One Modeling Framework for Integrated Task (OMFIT, [44]) is an integrated modeling and experimental data analysis software for magnetically confined thermonuclear fusion experiments. It allows easy data exchange among different codes [45]; in the case of this work, CHEASE and MARS-F.
OMFIT is a Python, object-based framework with its own data structures. All the tasks are coded in Python and different tasks nested in different trees can be called together or call each other, to create a complex workflow. OMFIT features a top-level GUI. Python classes are also defined within OMFIT: these are Python scripts loaded when OMFIT is launched and contain the definition of data types and methods which can be applied to a given object. For example, the class OMFITchease contains all the methods (such as plot, saving, smoothing, etc.) applied to an OMFITchease object (usually, this is the CHEASE input or output file).

CHEASE and MARS-F in the OMFIT framework

In the OMFIT framework CHEASE and MARS-F are integrated as modules. Two different versions of CHEASE have been developed:

- a *standard* version, which was used in this work to switch among different coordinate conventions [46] and manipulate equilibria
- a dedicated version developed to prepare the mesh and the input for the MARS-F code

Input files can be either a CHEASE specific (EXPEQ) or EQDSK (US standard) files. EXPEQ and EQDSK files are handled in OMFIT by the *OMFITchease* and *OMFITeqdsk* classes respectively. While the EQDSK presents more data, such as the pressure profile, the safety factor profile (both as a function of a normalized radius), the EXPEQ file presents the source terms profiles and is, besides, the type of file suitable to perform the insertion of a wall.
One of the main features of CHEASE is the transformation of the equilibrium. A single solution of the Grad-Shafranov equation can be rescaled to generate a whole sequence of equilibria with fixed poloidal beta and internal inductance, but with different plasma current values, rotational transform and toroidal beta. In CHEASE these transformations allow the generation of equilibria with prescribed values of either the total current or of the safety factor at some arbitrary flux surface ψ_q.
It must be noted that CHEASE has its own units: some quantities taken as inputs (for example the total plasma current) should be passed not in SI units, but with a normalized value. More about this normalization is reported in [42] and [47]. The CHEASE version developed to interface with MARS internally uses coordinate conventions (COCOS, [46]) equal to 2.

APPENDIX B

OMFIT WORKFLOWS

The workflows of the three different types of scans performed to obtain the results presented in this work are shown below. Figure 53 features the workflow followed to perform the pressure scan in order to obtain the no-wall limit $beta_N^{No-wall}$.

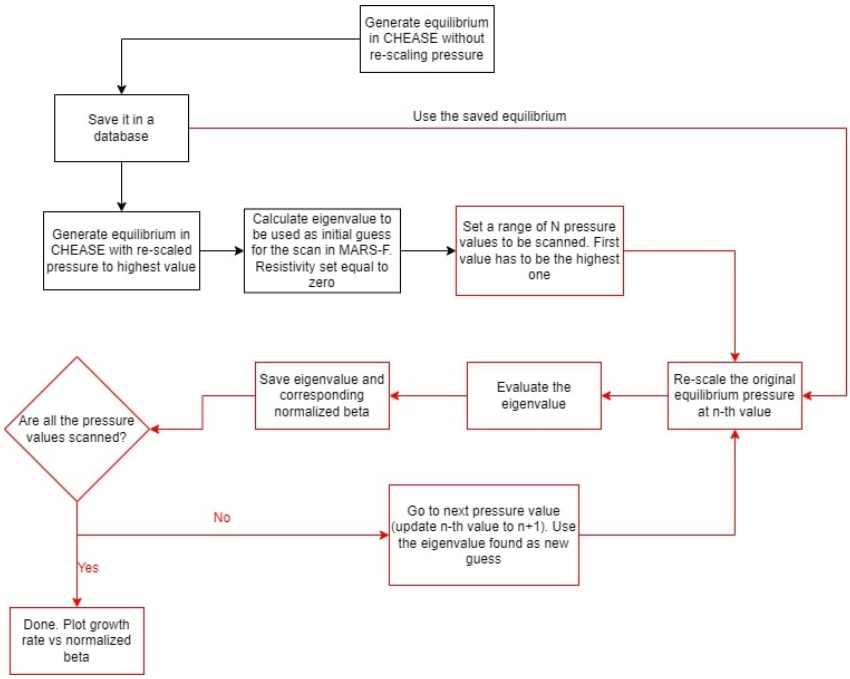

Figure 53: No-wall limit pressure scan workflow.

Figure 54 presents the workflow adopted to perform the pressure scan in order to evaluate the growth rate as function of pressure for non ideal plasmas.
Finally, figure 55 depicts the workflow for performing a resistivity scan, in order to obtain the dependence of the growth rate as function of resistivity/Lundquist number.

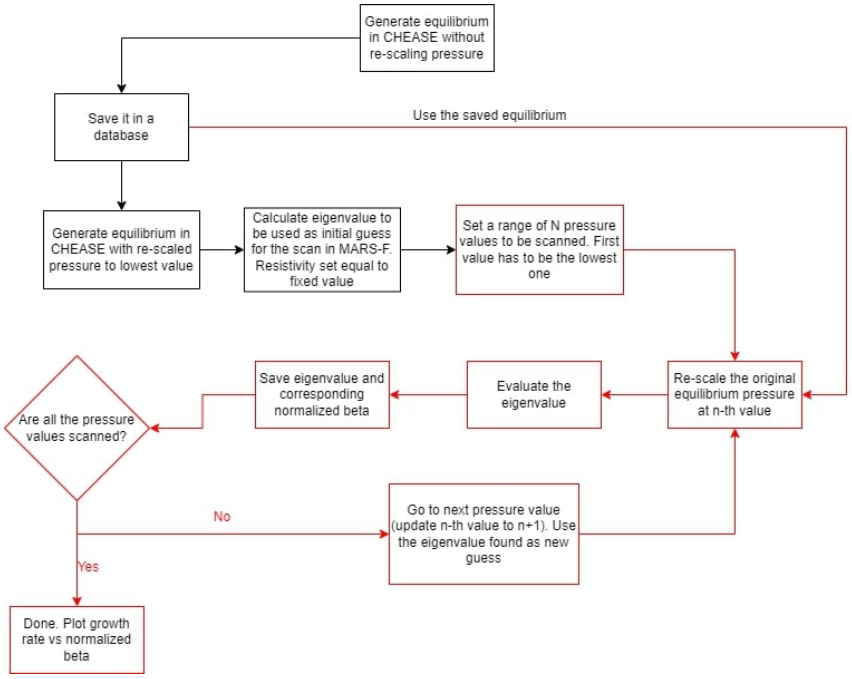

Figure 54: Resistive plasmas pressure scan workflow.

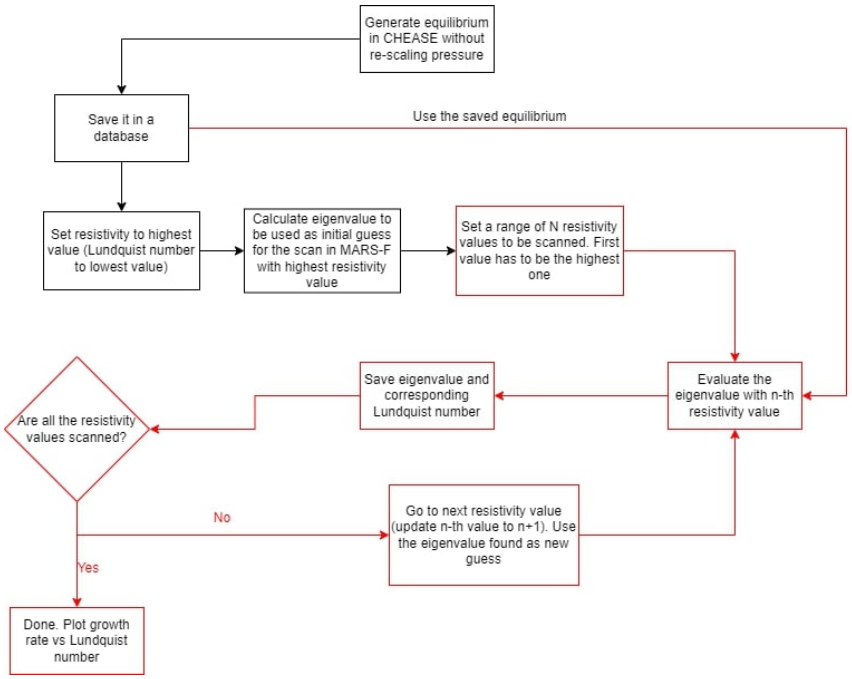

Figure 55: Resistivity scan workflow.

APPENDIX C

RESISTIVITY IMPLEMENTATION IN MARS-F

While performing the analyses, two different resistivity models have been adopted: the classical Spitzer model and a radial grid based resistivity profile generated by MARS-F. The radial grid based model implemented in MARS-F is the following:

$$\eta = \frac{\eta_0}{(R_0/a)^2} \frac{1}{1 + (\sigma_1 + \sigma_2 \psi_p)\psi_p}$$

where η_0 is the resistivity value at the magnetic axis, which is passed as input in the MARS-F namelist; this value corresponds to the inverse of the Lundquist number. R_0/a is the plasma aspect ratio. Also σ_1 and σ_2 are MARS-F input parameters. In this work, both were set to zero, thus leading to a constant resistivity profile along the normalized radius.
The Spitzer model implemented in MARS-F is:

$$\eta = \frac{\eta_0}{(R_0/a)^2} \left(\frac{T_e}{T_{e,0}} \right)^{-3/2}$$

where $T_{e,0}$ is the electron temperature value at magnetic axis. This model required the electron temperature profile as function of normalized radius to be taken as input.

BIBLIOGRAPHY

[1] F. C. Chen. *Introduction to Plasma Physics and Controlled Fusion, Vol.I: Plasma Physics*. 2nd edition, 1984.

[2] Hans Peter Goedbloed; Stefaan Poedts; Rony Keppens. *Magnetohydrodynamics of Laboratory and Astrophysical Plasmas*. 1st edition, 2019.

[3] Jeffrey P. Freidberg. *Plasma Physics and Fusion Energy*. Cambridge University Press, 1st edition, 2007.

[4] Lyman Spitzer Jr. *Physics of Fully Ionized Gases*. New York, Interscience Publishers, 2nd edition, 1962.

[5] J. Wesson. *Tokamaks*. Oxford University Press, 3rd edition, 2004.

[6] Jeffrey P. Freidberg. *Ideal Magnetohydrodynamics*. Cambridge University Press, 2nd edition, 2014.

[7] M. N. Bussac; R. Pellat; D. Edery; J. L. Soule. Internal kink modes in toroidal plasmas with circular cross sections. *Physical Review Letters*, 35(24):1638, 1975.

[8] A. Marinoni; M. E. Austin et al. H-mode grade confinement in L-mode edge plasmas at negative triangularity on DIII-D. *Physics of Plasmas*, 26:042515, 2019.

[9] A. H. Glasser; J. M. Greene; J. L. Johnson. Resistive instabilities in a tokamak. *The Physics of Fluids*, 19(4):567–574, 1976.

[10] A. Bondeson; G. Vlad; H. Lütjens. Global, resistive stability analysis in axisymmetric systems. *Controlled Fusion and Plasma Physics*, 1990.

[11] ASDEX Team (1989). The H-mode of ASDEX. *Nuclear Fusion*, 29(11), 1959.

[12] M. Greenwald. Density limits in toroidal plasmas. *Plasma Physics and Controlled Fusion*, 44(8), 2002.

[13] P. N. Yushmanov; T. Takizuka; K. S. Riedel; O. J. W. F. Kardaun; J. G. Cordey; S. M. Kaye; D. E. Post. Scalings for tokamak energy confinement. *Nuclear Fusion*, 30(10):1807–1818, 1990.

[14] ITER Global Data Base working group. IAEA-CN-69/ITERP1/7, paper presented at 17th IAEA conference on fusion energy, 1998.

[15] J.-M. Moret; S. Franke; H. Weisen; M. Anton; R. Behn; B. P. Duval; F. Hofmann; B.Joye; Y. Martin; C. Nieswand; Z. A. Pietrzyk; W. van Toledo. Influence of plasma shape on transport in the TCV tokamak. *Physics Review Letters*, 79(11):2057–2060, 1997.

[16] A. Pochelon; P. Angelino et al. Recent TCV results - Innovative plasma shaping to improve plasma properties and insight. *Plasma and Fusion Research*, 7:2502148–2502148, 2012.

[17] EuroFusion. TCV Wiki. https://wiki.euro-fusion.org/wiki/WPTE_TCV, 2022.

[18] F. Troyon; R. Gruber; H. Saurenmann; S. Semenzato; S. Succi. MHD limits to plasma confinement. *Plasma Physics and Controlled Fusion*, 26(1A):209–215, 1984.

[19] A. Pochelon; T. P. Goodman et al. Energy confinement and MHD activity in shaped TCV plasmas with localized electron cyclotron heating. *Nuclear Fusion*, 39(11):2057–2060, 1999.

[20] Y. Camenen; A. Pochelon; R. Behn; A. Bottino; A-Bortolon; S. Coda; A. Karpushov; O. Sauter; G. Zhuang and the TCV team. Impact of plasma triangularity and collisionality on electron heat transport in TCV L-mode plasmas. *Nuclear Fusion*, 47:510–516, 2007.

[21] A. Marinoni; S. Brunner; Y. Camenen; S. Coda; J. P. Graves; X. Lapillonne; A. Pochelon; O. Sauter; L. Villard and the TCV team. The effect of plasma triangularity on turbulent transport: modeling TCV experiments by linear and non-linear gyrokinetic simulations. *Plasma Physics and Controlled Fusion*, 51(5):055016, 2009.

[22] M. E. Austin; A. Marinoni; M. L. Walker; M. W. Brookman; J. S. deGrassie; A. W. Hyatt; G. R. McKee; C. C. Petty; T. L. Rhodes; S. P. Smith; C. Sung; K. E. Thome; A. D. Turnbull. Achievement of reactor-relevant performance in negative triangularity shape in the DIII-D tokamak. *Physical Review Letters*, 122:115001, 2019.

[23] A. Merle; S. Yu. Medvedev; O. Sauter. Pedestal properties of H-modes with negative triangularity using EPED-CH model. *Plasma Physics and Controlled Fusion*, 59:104001, 2017.

[24] M. Kikuchi; T. Takizuka; S. Yu. Medvedev; T. Ando; D. Chen; J. X. Li; M. Austin; O. Sauter; L. Villard; A. Merle; M. Fontana; Y. Kishimoto; K. Imadera. L-mode-edge negative triangularity tokamak reactor. *Nuclear Fusion*, 59(5):056017, 2019.

[25] S. Yu. Medvedev; M. Kikuchi; L. Villard; T. Takizuka; P. Diamond; H. Zushi; K. Nagasaki; X. Duan; Y. Wu; A. A. Ivanov; A. A. Martynov; Yu.

Yu. Poshekhonov; A. Fasoli; O. Sauter. The negative triangularity tokamak: stability limits and prospects as fusion energy system. *Nuclear Fusion*, 55(6):063013, 2015.

[26] Jing Ren; Yueqiang Liu; Yue Liu; S. Yu. Medvedev; Zhirui Wang; Guoliang Xia. A comparative study of ideal kink stability in two reactor-relevant tokamak plasma configurations with negative and positive triangularity. *Plasma Physics and Controlled Fusion*, 58(11):115009, 2016.

[27] A. Marinoni; M. E. Austin et al. Diverted negative triangularity plasmas on DIII-D: the benefit high confinement without the liability of an edge pedestal. *Nuclear Fusion*, 61(11):116010, 2021.

[28] S. Coda; A. Merle; O. Sauter; L. Porte; F. Bagnato; J. Boedo; T. Bolzonella; O. Février; B. Labit; A. Marinoni; A. Pau; L. Pigatto; U. Sheikh; C. Tsui; M. Vallar; T. Vu and the TCV team. Enhanced confinement in diverted negative-triangularity L-mode plasmas in TCV. *Plasma Physics and Controlled Fusion*, 64(1):014004, 2021.

[29] F. Hofmann et al. Creation and control of variably shaped plasmas in TCV. *Plasma Physics and Controlled Fusion*, 36:B277, 1994.

[30] S. Coda et al. Physics research on the TCV tokamak facility: from conventional to alternative scenarios and beyond. *Nuclear Fusion*, 59:112023, 2019.

[31] M. Spolaore et al. H-mode achievement and edge features in RFX-mod tokamak operation. *Nuclear Fusion*, 57:116039, 2017.

[32] I. Predebon; D. Abate; L. Pigatto. Positive and negative triangularity in RFX-mod2: a comparative analysis. *Nuclear Fusion*, 62:066039, 2022.

[33] M. Zuin. Overview of the RFX-mod fusion science activity. *Nuclear Fusion*, 57:102012, 2017.

[34] EuroFusion. TSVV-02 Wiki. https://wiki.euro-fusion.org/wiki/TSVV-02, 2022.

[35] R. Iacono; A. Bhattacharjee; C. Ronchi; J. M. Greene; M. H. Hughes. Stability of tearing modes in finite-beta plasmas. *Physics of Plasmas*, 1(8):2645–2652, 1994.

[36] W. Guo; J. Ma. Numerical study of flow effect on internal kink mode in finite beta plasmas. *AIP Advances*, 10(7), 2020.

[37] EuroFusion. Rt07: Negative Triangularity scenarios as an alternative for DEMO Wiki. https://wiki.euro-fusion.org/wiki/WPTE_wikipages:_Experimental_campaign_2021:RT07, 2022.

[38] L. Pigatto; T. Bolzonella; A. Piras; S. Coda; A. Merle; C. Piron; L. Porte; O. Sauter; M. Vallard and the TCV team. Global stability and MHD dynamics in TCV negative triangularity plasmas. *48th EPS Conference on Plasma Physics. European Physical Society.*

[39] G. Z. Hao; Y. Q. Liu; A. K. Wang; Y. Sun; Y. H. Xu; H. D. He; M. Xu; H. P. Qu; X. D. Peng; J. Q. Xu; S. Y. Cui; X. M. Qiu. Finite toroidal flow generated by unstable tearing mode in a toroidal plasma. *Physics of Plasmas*, 21:122503, 2014.

[40] D. Abate; G. Marchiori; P. Bettini; F. Villone. Modelling of RFX-mod2 tokamak equilibria with demo-like shape conditions and negative triangularity. *Plasma Physics and Controlled Fusion*, 62:085001, 2020.

[41] Y. Liu. Manual for running MARS-* series. Version 1.6. *General Atomics internal publication*, 2010.

[42] H. Lütjens; A. Bondeson; O. Sauter. The CHEASE code for toroidal MHD equilibria. *Computer Physics Communication*, 97(3):219–260, 1996.

[43] Y. Q. Liu; A. Bondeson. Feedback stabilization of nonaxisymmetric resistive wall modes in tokamaks. I. Electromagnetic model. *Physics of Plasmas*, 7(9), 2000.

[44] OMFIT website. https://www.omfit.io/, 2022.

[45] O. Meneghini; L. Lao. Integrated Modeling of Tokamak Experiments with OMFIT. *Plasma and Fusion Research*, 8:2403009, 2013.

[46] O. Sauter; S. Yu. Medvedev. Tokamak Coordinate Conventions: COCOS. *Computer Physics Communications*, 184(2):293–302, 2013.

[47] O. Sauter. Normalizations on CHEASE. https://crppwww.epfl.ch/~sauter/chease/chease_normalization.pdf, 2013.

This work has been carried out within the framework of the EUROfusion Consortium, funded by the European Union via the Euratom Research and Training Programme (Grant Agreement No. 101052200 - EUROfusion). Views and opinions expressed are however those of the author only and do not necessarily reflect those of the European Union or the European Commission. Neither the European Union nor the European Commission can be held responsible for them.
Part of the data analysis was performed using the OMFIT integrated modeling framework.

DECLARATION

This work is my intellectual property.

Torino, Academic Year 2021/2022

Anthony Piras